

# Anisotropic In-plane Thermal Conductivity of Freestanding Few-layer ReS<sub>2</sub>

Manavendra Pratap Singh<sup>1</sup>, Akshay Naik<sup>1\*</sup>

<sup>1</sup>Centre for Nano Science and Engineering, Indian Institute of Science,

Bengaluru, Karnataka 560012, India

\*Corresponding author: [anaik@iisc.ac.in](mailto:anaik@iisc.ac.in)

## Abstract:

Rhenium disulfide (ReS<sub>2</sub>) is a unique TMDC with a strong in-plane anisotropy and weak interlayer coupling. The pronounced anisotropy in the thermal conductivity observed in bulk ReS<sub>2</sub> flakes (exceeding 60 nm) makes them valuable for applications that require directional heat management or isolation. Whether this anisotropy is maintained below 10 nm has not yet been studied. Here, we measured the thermal conductivity of freestanding, exfoliated, few-layer ReS<sub>2</sub> samples (thickness < 10 nm) on SiO<sub>2</sub>/Si holey substrates using the optothermal Raman technique. Polarization-dependent Raman measurements revealed variation in thermal conductivity along the high symmetry axes. The total in-plane thermal conductivities show a nonmonotonic trend with ReS<sub>2</sub> thickness ranging from 2.5 to 8 nm. The in-plane thermal conductivity of few-layer ReS<sub>2</sub> devices, which varies with thickness, holds significant potential for applications in nanoscale thermoelectric devices.

**Keywords:** Freestanding ReS<sub>2</sub>, Polarization-dependent Raman spectroscopy, Anisotropic thermal conductivity.

## Introduction:

Transition-metal dichalcogenides (TMDCs) have demonstrated extraordinary optoelectronic and thermal properties<sup>1-4</sup>. These properties make them ideal for many nanoscale device applications. Layered TMDCs such as MoS<sub>2</sub>, MoSe<sub>2</sub>, WS<sub>2</sub>, and WSe<sub>2</sub> have a direct bandgap in the monolayer limit and have been explored for piezotronics and optoelectronic applications<sup>5-10</sup>. In contrast, TMDCs such

as ReS<sub>2</sub> have weak interlayer coupling owing to the Peierls distortion of the octahedral (1T) structure of ReS<sub>2</sub><sup>11-13</sup>, resulting in a distorted 1T (1T') structure. The 1T' structure of ReS<sub>2</sub> is shown in Figure 1a. The direction of the Re chains defines the *b*-axis of the crystal, as indicated by an arrow. This distorted structure results in weak interlayer coupling, which makes ReS<sub>2</sub> a direct-bandgap semiconductor (1.55 eV), regardless of the layer thickness<sup>11</sup>. Furthermore, ReS<sub>2</sub> has two stable stacking orders (AA and AB) (Figure 1a), which show different optical and vibrational properties<sup>14-17</sup>.

Previous studies have reported strong in-plane anisotropy, resulting in directional optical and electrical properties of bulk and few-layer ReS<sub>2</sub><sup>18-21</sup>. Other anisotropic materials, including Black Phosphorus (BP) and Td-WTe<sub>2</sub>, show significant in-plane variations<sup>22,23</sup>. Td-WTe<sub>2</sub> have thermal conductivity of 0.743 and 0.639 W/m-K along the zigzag and armchair axes<sup>22</sup>. Zhe *et al.* reported the impact of anisotropic phonon dispersion on thermal conductivities, with values of approximately 10 W/m-K and 20 W/m-K for zigzag and armchair configurations, respectively, in a ~10 nm thick BP flake<sup>23</sup>. Similar anisotropic behaviors have also been detected in the thermal studies of ReS<sub>2</sub><sup>24,25</sup>.

However, only a limited number of experimental studies have been conducted on the thermal conductivity of ReS<sub>2</sub>. Jang *et al.* first determined the orientation-dependent thermal conductivity of the exfoliated ReS<sub>2</sub> flakes with 60-450 nm thicknesses using time-domain thermoreflectance (TDTR)<sup>24</sup>. The in-plane thermal conductivity is higher along the *b*-axis (along the Re chains) than along the cross *b*-axis (transverse to the Re chains). Recently, Tahbaz *et al.* also reported the anisotropic thermal conductivity of ReS<sub>2</sub> using frequency domain thermoreflectance (FDTR) for a flake thickness of ~3 μm<sup>25</sup>. Both these studies focused on substrate-supported ReS<sub>2</sub>, where the substrate can influence the thermal conductivity of ReS<sub>2</sub>. An extensive study on the thermal conductivity of freestanding ReS<sub>2</sub>, particularly for thicknesses below the 10 nm threshold, is currently lacking. Such studies are crucial for the development of nanoscale devices for thermal transport, isolation, and anisotropic heat management.

In this work, we used optothermal techniques to measure the thermal conductivity of mechanically exfoliated ReS<sub>2</sub> flakes. The thickness of the flakes ranges from 2.5 nm to 8 nm. To reduce the effect of the substrate underneath, these samples were prepared on holes in the substrate. To identify the

crystallographic  $b$ -axis and cross  $b$ -axis of the samples, we examined the polarization dependence of the Raman Spectra. We calculated the anisotropic in-plane thermal conductivities using the temperature- and power-dependent Raman spectra acquired along the  $b$ -axis and cross  $b$ -axis. For these freestanding ReS<sub>2</sub> flakes, the in-plane thermal conductivities are observed to be  $51 \pm 5$  and  $39 \pm 2$  W/m-K along the  $b$ -axis and cross  $b$ -axis, respectively, for a thickness of  $\sim 3.5$  nm. We also examined the impact of the two stacking orders (AA and AB) of ReS<sub>2</sub> on the thermal conductivity. The thickness-dependent in-plane thermal conductivities were nonmonotonic. The results presented in this study are useful for the design and development of novel devices that leverage the anisotropic thermal properties of ReS<sub>2</sub>.

### **Results and discussion:**

The substrate in this measurement was a 290 nm SiO<sub>2</sub> on top of a silicon wafer. An array of holes is created on this substrate using optical lithography and reactive ion etching (RIE) (see Supporting Information S1 for more details). Commercially procured few-layer ReS<sub>2</sub> flakes were mechanically exfoliated onto polydimethyl siloxane (PDMS) and then transferred onto the array of holes fabricated on a SiO<sub>2</sub>/Si substrate via a dry transfer technique<sup>26</sup> (see Methods). Figure 1b shows an optical image of the ReS<sub>2</sub> flake on the "holey" substrate of SiO<sub>2</sub>/Si. The thickness ( $\sim 3.5$ ) of the transferred flake was measured using atomic force microscopy (AFM) at the edge of the flake (Figure 1c).

Figure 1d shows a simplified schematic of the experimental setup for optothermal Raman measurements. Figure 1e compares the Raman spectra of the ReS<sub>2</sub> flake acquired from the supported (on the substrate) and freestanding regions highlighted in Figure 1b. All the previously reported prominent Raman-active vibrational modes of ReS<sub>2</sub> are observed<sup>12</sup>. Here, we show only the first six Raman modes from 120 to 240 cm<sup>-1</sup>, labeled as I, II, III, IV, V, and VI. The extended Raman spectra are presented in Supporting Information S2. There are prominent differences between the spectra observed for ReS<sub>2</sub> on the substrate and holes. There is a red shift for all the Raman modes when the measurements are performed on ReS<sub>2</sub> on holes compared to when on the substrate. This redshift has previously been attributed to tensile strain<sup>27,28 29</sup>. The intensities of all the Raman mode peaks for the freestanding region

are higher than those for the supported region. Additionally, the photoluminescence (PL) intensity of ReS<sub>2</sub> (Figure 1f) acquired from the hole region was ~6 times greater than that of the SiO<sub>2</sub>-supported region. The Raman and PL intensity enhancements on the holes further confirm the freestanding nature<sup>30,31</sup>.

ReS<sub>2</sub> is known to have two different stacking orders, which are likely to influence its thermal conductivity. To identify whether the stacking order is AA or AB, we use the separation between Raman modes I and III<sup>14,15,32</sup>. For monolayer ReS<sub>2</sub>, the peak separation was ~ 17 cm<sup>-1</sup>. The separation was less than that for AA stacking, and for AB stacking, it was more<sup>14,15</sup>. The separation between Raman modes III and I of the flake is 14.02 cm<sup>-1</sup>, which confirms the AA stacking order (see Supporting Information S3).

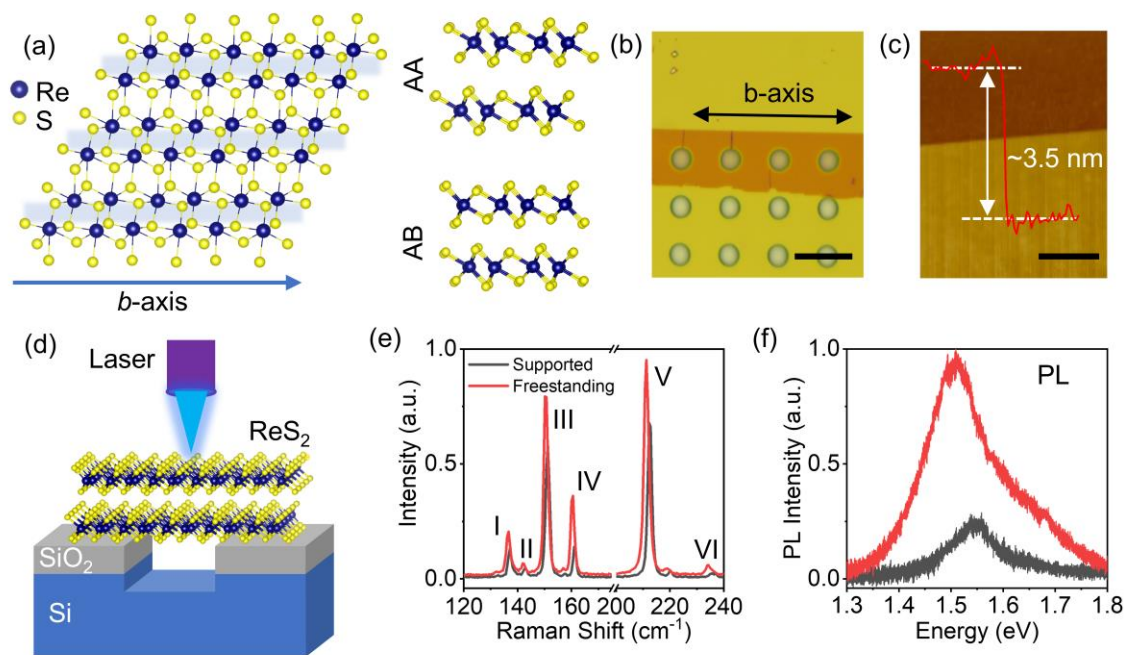


**Figure 1.** (a) Top view of the crystal structure of the ReS<sub>2</sub> monolayer. The direction of the Re chains (*b*-axis) is highlighted. Side views of AA and AB stacked bilayer ReS<sub>2</sub> are shown. (b) Optical micrograph of ~3.5 nm ReS<sub>2</sub> flake on the array of holes in SiO<sub>2</sub>/Si substrate. The flake has a sharp edge along the *b*-axis, which is denoted by a double-headed arrow (black). The scale bar is 10 μm. (c) AFM image of the sample's edge and height profile. The scale bar is 1 μm. (d) Schematic representation of the

*experimental setup for the optothermal Raman technique. Point Raman and PL spectra from the supported and freestanding regions of the ReS<sub>2</sub> flake are plotted in (e) and (f), respectively.*

ReS<sub>2</sub> is an anisotropic material, which indicates that we should expect variation in the Raman response with crystallographic orientation. To determine the orientation, we performed angle-resolved polarized Raman measurements on the ReS<sub>2</sub> flakes (with less than  $\pm 2$  angular uncertainty). The sample was rotated by an angle ( $\theta$ ) between the incident laser polarization and the cleaved edge (indicated by a black double-headed arrow in Figure 2a). The scattered Raman light was collected into the spectrometer without additional polarization optics. Raman spectra for different angles are shown in Figure 2b. As expected, the Raman peak positions of different modes remain unchanged, but the intensity varies with the angle. Recent studies indicate that mode V has maxima along the Re-chain axis (also called the b-axis)<sup>18,33</sup>. Figure 2c shows a polar plot of the Raman intensity of modes III and V of the ReS<sub>2</sub> flake (Figure 2a). Modes V and III show maximum Raman intensities at  $\sim 5^\circ$  and  $\sim 35^\circ$ , respectively, which enables us to identify the b-axis of our sample.

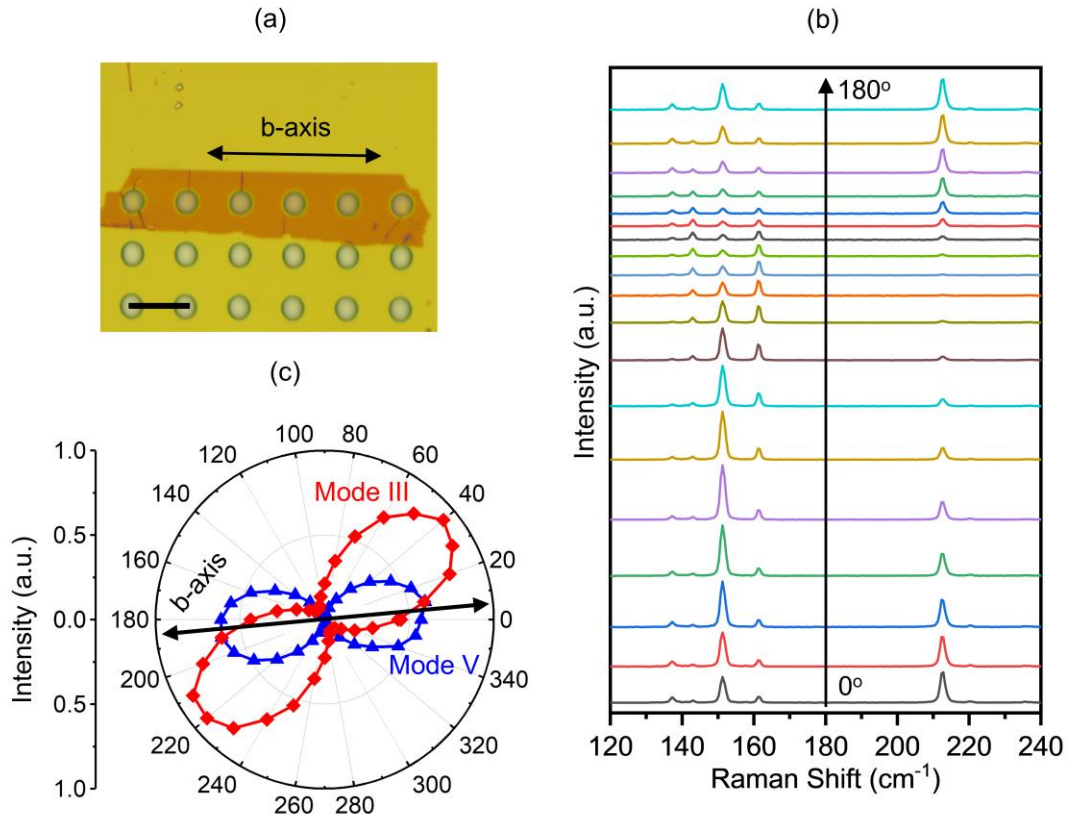


**Figure 2.** (a) Optical micrograph of  $\sim 3.5$  nm  $\text{ReS}_2$  flake on the array of holes in  $\text{SiO}_2/\text{Si}$  substrate. The flake has a sharp edge along the  $b$ -axis. The scale bar is  $10\ \mu\text{m}$ . (b) Unpolarized Raman spectra as a function of the sample orientation angle ( $0^\circ$  to  $180^\circ$  in steps of  $10^\circ$ ). (c) Polar plot of the Raman intensities of modes III (red) and V (blue).

To measure the thermal conductivity of freestanding  $\text{ReS}_2$ , we used the optothermal Raman technique<sup>34,35</sup>. This technique uses the laser power and temperature-dependent shifts of the Raman modes to estimate the thermal conductivities of freestanding 2D materials. In the case of substrate-supported samples, the substrate underneath can significantly influence the thermal properties of 2D materials. This is mediated by substrate defects, phonon-boundary scatterings, and heat dissipation through the substrate<sup>36,37</sup>. We did not observe any substantial shift in the peak position of Raman spectra on substrate-supported  $\text{ReS}_2$  in the laser power-dependent measurement owing to faster heat dissipation through  $\text{SiO}_2/\text{Si}$ <sup>35</sup> (see Supporting Information S4 for details). The substrate ( $\text{SiO}_2/\text{Si}$ ) effect can be eliminated using freestanding  $\text{ReS}_2$  for thermal conductivity measurements. In our measurement, the

laser was focused at the center of the freestanding ReS<sub>2</sub> flake, and the measurement showed a shift in Raman modes with the change in incident laser power.

The measured thermal conductivity was not dependent on the Raman modes chosen for the calculation<sup>38</sup>. The Raman mode, which is most sensitive to laser power and temperature change, is preferred to measure the anisotropic thermal conductivity. Mode V shows the largest red shifts with laser power and temperature. Therefore, this mode was selected to calculate the anisotropic thermal conductivity of ReS<sub>2</sub>.

The laser power and temperature-dependent Raman spectra of mode V for the ~3.5 nm freestanding ReS<sub>2</sub> along the *b*-axis and cross *b*-axis are shown in Figure 3a-b and Figure 3c-d, respectively. All Raman modes of the freestanding ReS<sub>2</sub> were redshifted with increasing laser power or temperature. The accurate peak positions of the Raman modes were extracted by Voigt function fitting. In Figure 3e, the power-dependent shift of mode V along the *b*-axis and the cross *b*-axis is characterized by the expression,

$$\Delta\omega = \omega(P_2) - \omega(P_1) = \gamma\Delta P \quad (1)$$

where  $\gamma$  is the slope ( $\delta\omega/\delta P$ ) of the power dependence of the Raman peak position in the linear region and is called the first-order power coefficient. The extracted first-order power coefficient of mode V is found to be  $-10.89 \pm 0.22 \text{ cm}^{-1}/\text{mW}$  along the *b*-axis and  $-7.99 \pm 0.24 \text{ cm}^{-1}/\text{mW}$  along the cross *b*-axis.

Similarly, the temperature-dependent frequency shift of mode V along the *b*-axis and cross *b*-axis for ~3.5 nm ReS<sub>2</sub> shows a linear trend (Figure 3f). The first-order temperature coefficient is extracted using the equation<sup>39,40</sup>,

$$\omega(T) = \omega_0 + \chi T \quad (2)$$

where  $\omega_0$  is the frequency of mode V at absolute zero temperature, and  $\chi$  is the first-order temperature coefficient of the Raman mode V. For the ~3.5 nm thick flake, the extracted temperature coefficients were  $\chi_{b, mode V} = -(1.23 \pm 0.10) \times 10^{-2} \text{ cm}^{-1}/\text{K}$  and  $\chi_{\perp b, mode V} = -(0.69 \pm 0.02) \times 10^{-2} \text{ cm}^{-1}/\text{K}$ . The

temperature coefficient along the b-axis is observed to have a larger value than the cross b-axis due to anisotropic thermal expansion during the heating process<sup>23</sup>.

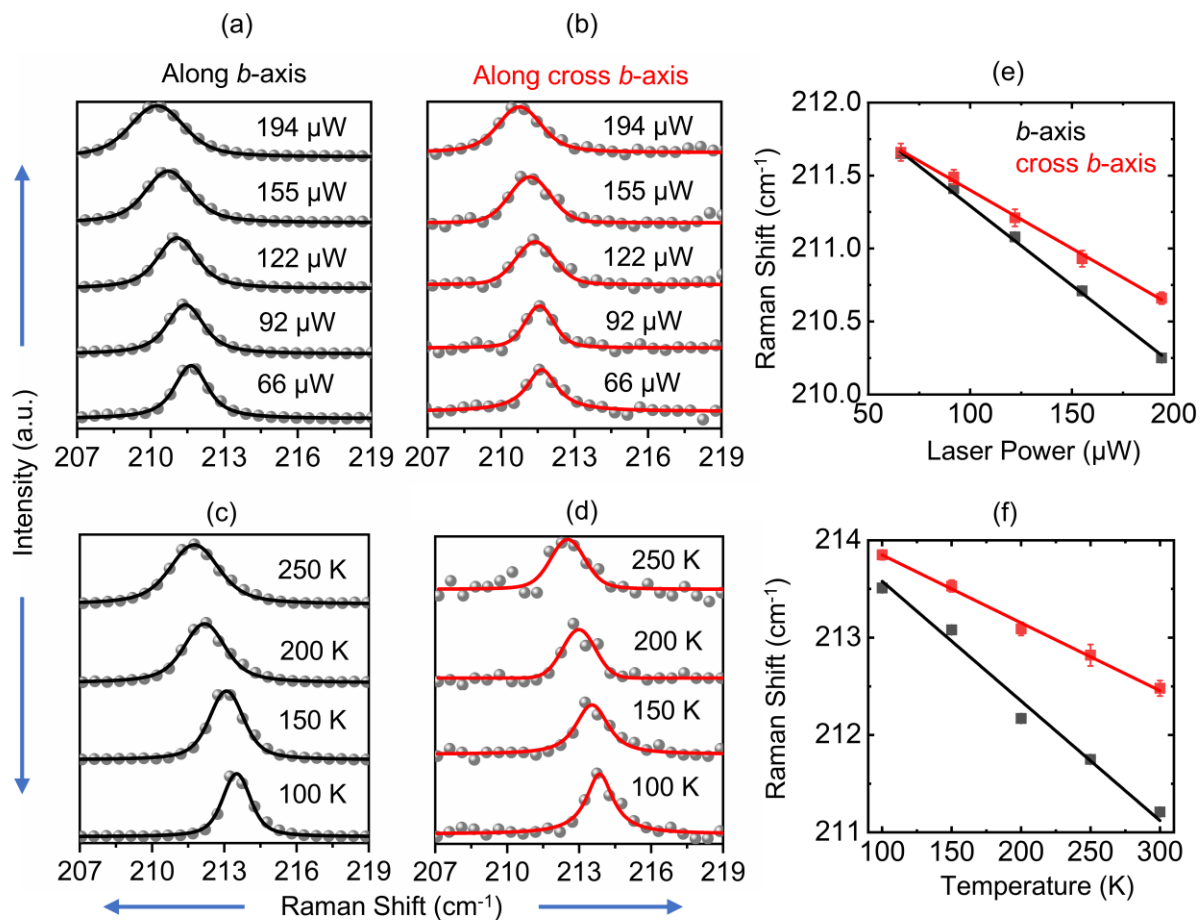


**Figure 3.** Power-dependent  $\mu$ -Raman spectra of mode  $V$  for  $\sim 3.5$  nm thick  $\text{ReS}_2$  (AA) along the (a)  $b$ -axis and (b) cross  $b$ -axis. Temperature-dependent micro-Raman spectra of mode  $V$  of the same sample along (c)  $b$ -axis and (d) cross  $b$ -axis. (e) Raman peak position vs. laser power plot extracted from the Voigt function fitting of (a) and (b). The lines (red and black) are linear fitting to obtain the first-order power coefficient. (f) Raman peak position vs. laser power plot extracted from the Voigt function fitting of (c) and (d). The lines (red and black) are linear fitting to obtain the first-order temperature coefficient.

The expression for the thermal conductivity can be derived from the heat conduction equation:

$$\frac{\partial Q}{\partial t} = -\kappa \oint \nabla T \cdot dA \quad (3)$$

$\frac{\partial Q}{\partial t}$  is the thermal power flowing through a cross-sectional area,  $\nabla T$  is the temperature gradient, and  $\kappa$  is the thermal conductivity of the sample. Assuming radial heat flow from the center to the edge of the freestanding area, the above equation results in the expression<sup>34</sup>:

$$\kappa = \frac{1}{2\pi h} \frac{\Delta P}{\Delta T} \quad (4)$$

where,  $h$  is the thickness of the ReS<sub>2</sub> flake, and  $\Delta T$  is the change in temperature due to the change in heating power  $\Delta P$ . Using equation 2, the thermal conductivity expression can be modified as,

$$\kappa = \chi \left( \frac{1}{2\pi h} \right) \left( \frac{\delta\omega}{\delta P} \right)^{-1} \quad (5)$$

Using the experimentally determined values of first-order temperature coefficient and power coefficient, the thermal conductivities are calculated to be  $51 \pm 5$  W/m-K (*b*-axis), and  $39 \pm 2$  W/m-K (cross *b*-axis) for the  $\sim 3.5$  nm thick ReS<sub>2</sub> of AA stacking. The calculated  $\kappa_{b, \text{ mode V}}$  was higher than  $\kappa_{\perp b, \text{ mode V}}$ , indicating an anisotropic feature in the thermal conductivity. This originates mainly from anisotropic phonon dispersion<sup>23</sup>. Additionally, we have calculated the anisotropic thermal conductivity using mode III (see Supporting Information S5), which agrees with the mode V thermal conductivity.

To study the dependence of the stacking order on the thermal conductivity, we measured the thermal conductivity of another  $\sim 3.5$  nm ReS<sub>2</sub> sample with AB stacking (see Figure S6a). To find the *b*-axis, we performed angle-resolved polarized Raman measurements of the ReS<sub>2</sub> flake, similar to the previous sample (see Supporting Information S6 for more details). The laser power and temperature-dependent peak shifts of  $\sim 3.5$  nm ReS<sub>2</sub> (AB stacking) along the *b*-axis (black) and cross *b*-axis (red) are shown in Figure 4a and 4b, respectively (see Supporting Information S7 for more details). As previously done, the first-order power and temperature coefficients were extracted by linear fitting of those peak shifts. The slope  $\delta\omega/\delta P$  of mode V is found to be  $-12.6 \pm 0.40$  cm<sup>-1</sup>/mW (along *b*-axis) and  $-8.45 \pm 0.19$  cm<sup>-1</sup>/mW (along cross *b*-axis). The extracted temperature coefficients were  $\chi_{b, \text{ mode V}} = -(1.17 \pm 0.06) \times 10^{-2}$  cm<sup>-1</sup>/K and  $\chi_{\perp b, \text{ mode V}} = -(0.69 \pm 0.03) \times 10^{-2}$ . The calculated thermal conductivity of  $\sim 3.5$  nm ReS<sub>2</sub>

(AB stacking) is:  $\kappa_{b, \text{ mode } V} = 42 \pm 3 \text{ W/m-K}$ , and  $\kappa_{\perp b, \text{ mode } V} = 37 \pm 2 \text{ W/m-K}$  (Thermal conductivity calculation using mode III is presented in Supporting Information S8). Therefore, AB stacking of ReS<sub>2</sub> also shows anisotropic thermal conductivity. It was observed that the in-plane anisotropic thermal conductivity value of ReS<sub>2</sub> for AB stacking was slightly less than that of AA stacking for the same thickness.

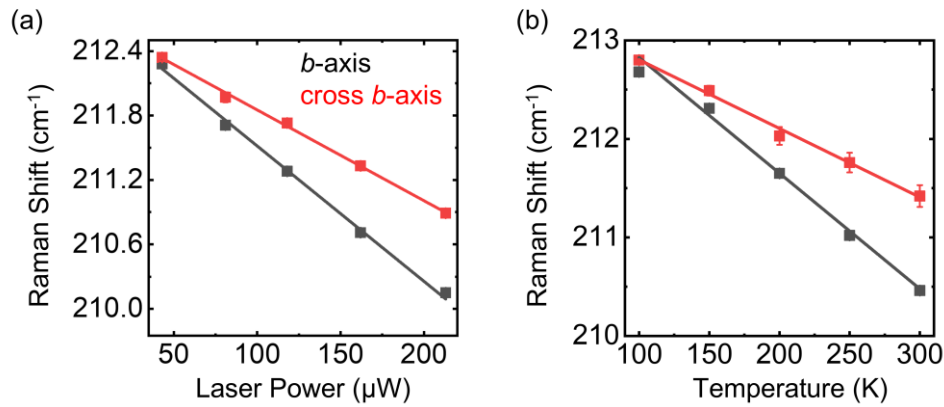


**Figure 4.** Raman peak position vs. (a) laser power and (b) temperature plots for mode *V* of ~3.5 nm ReS<sub>2</sub> (AB) along *b*-axis (black) and cross *b*-axis (red). The lines (red and black) are linear fitting to get the first-order power coefficient.

Previous thermal conductivity measurements on 2D materials have indicated a thickness dependence<sup>22,23,41-44</sup>. To understand this effect, we measured thermal conductivity on multiple samples of varying thicknesses (see Supporting Information S9-S12 for more details). We observed a clear nonmonotonic variation in thermal conductivity with thickness (Figure 5). The minimum thermal conductivity is observed at approximately 5-7 nm. This observation is consistent with the thermal conductivities of other 2D materials, including MoS<sub>2</sub><sup>41,42</sup>, BP<sup>23</sup>, and Td-WTe<sub>2</sub><sup>22</sup>. This decrease in thermal conductivity with thickness has previously been attributed to changes in the anharmonic force constant and phonon dispersion variations. In MoS<sub>2</sub>, the anharmonic force constant change is due to interlayer coupling-induced symmetry breaking. However, unlike the MoS<sub>2</sub> monolayer, monolayer ReS<sub>2</sub> has a distorted 1T phase, which lacks symmetry. Additional weak interlayers are unlikely to impact this force constant. This indicates that the initial reduction in thermal conductivity with increasing thickness of

ReS<sub>2</sub> is likely due to phonon dispersion changes. Theoretical calculations are required to clarify these effects. Beyond the minima, we also observe an increase in thermal conductivity, ultimately reaching close to bulk values at approximately 8 nm. For comparison, Figure 5 also presents the thermal conductivity values calculated by Jang et al. for thick ReS<sub>2</sub> flakes ranging from 60 to 450 nm using TDTR<sup>24</sup>, as well as by Tahbaz et al. using FDTR<sup>25</sup>. Although our values matched the reported bulk values, we did not observe large thermal conductivities along the *b*-axis, as reported by Tahbaz et al.

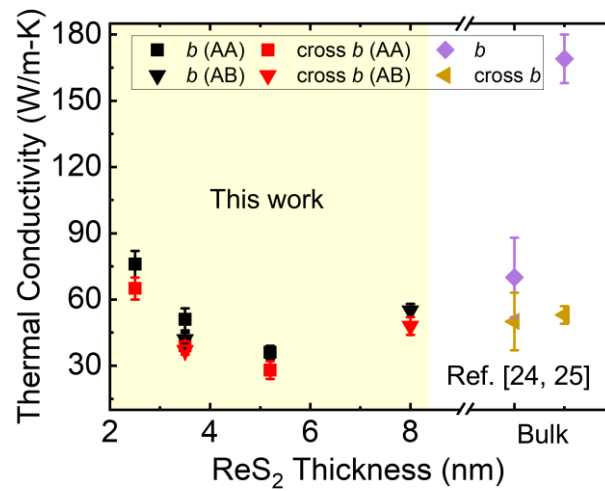


**Figure 5.** In-plane anisotropic thermal conductivity of ReS<sub>2</sub> flakes for thickness range 2.5 to 8 nm (this work) and bulk<sup>24,25</sup>. AA and AB represent the two different stacking modes in ReS<sub>2</sub>.

## Conclusion:

In conclusion, we experimentally measured the anisotropic in-plane thermal conductivity of freestanding few-layered ReS<sub>2</sub> using the optothermal Raman technique. Linear polarization-dependent Raman measurements were performed to identify the *b*-axis and cross *b*-axis of the samples. Then, temperature and power-dependent Raman spectra were acquired along the *b*-axis and cross *b*-axis. The extracted first-order temperature and power coefficients show a highly anisotropic response and are utilized to calculate the in-plane anisotropic thermal conductivity. The calculated thermal conductivities are  $51 \pm 5$  and  $39 \pm 2$  W/m-K along the *b*-axis and cross *b*-axis, respectively, for a  $\sim 3.5$  nm ReS<sub>2</sub> (AA stacking) thickness. These anisotropic in-plane thermal conductivities are the responses of the different

mean free paths of the phonons along the  $b$ -axis and cross the  $b$ -axis. A nonmonotonic variation was observed in the in-plane anisotropic thermal conductivity with a change in the thickness from 2.5 to 8 nm, which we attribute to phonon dispersion and changes in scattering mechanisms. Unlike MoS<sub>2</sub>, ReS<sub>2</sub> monolayer lacks the symmetry. This implies that anharmonic force constant change is unlikely to play a role in thermal conductivity variation with thickness. Further theoretical and experimental studies are required to elucidate the exact mechanism that controls these properties.

This study establishes a quantitative understanding of anisotropic and thickness-dependent thermal transport in ReS<sub>2</sub>. It provides critical insights into engineering thermal flow in nanoscale devices and has potential applications in thermal diodes, anisotropic thermoelectric devices, and other platforms that require directional heat flow.

#### **Methods:**

We follow the protocol for the dry transfer of 2D materials used by Castellanos-Gomez *et al.*<sup>26</sup>. ReS<sub>2</sub> flakes were mechanically exfoliated from bulk crystals (2D semiconductors) using blue tape onto a stamp. The stamp was a thin layer of a commercially available viscoelastic material (Gel-Film from Gel-Pak). Then, the selected flake on the stamp was dry-transferred onto the array of holes made in the SiO<sub>2</sub>/Si substrate using a 2D material transfer system.

AFM (Park NX20) was used to measure the depth of the holes and thicknesses of the ReS<sub>2</sub> flakes. Raman and PL measurements were performed using Horiba Scientific Lab RAMHR 800 in backscattering geometry. A 532 nm solid-state diode laser with 0.04 to 0.5 mW power and a  $\sim 0.5$   $\mu\text{m}$  spot size was focused onto the substrate using a 100 $\times$  objective. The laser power was chosen as a compromise between a reasonable signal-to-noise ratio (SNR) and laser-induced heating in the ReS<sub>2</sub> flakes during temperature-dependent measurements.

## Supporting Information:

Fabrication of the holey substrate; optical images, AFM, and Raman characterization of the ReS<sub>2</sub> samples; confirmation of AA and AB stackings of ReS<sub>2</sub>; laser power and temperature-dependent Raman spectra; first-order power coefficients, temperature coefficients, and anisotropic thermal conductivities of ReS<sub>2</sub> samples using modes III and V; tabulation of the anisotropic thermal conductivities.

## Author information:

Corresponding Author: \*Akshay Naik, [anaik@iisc.ac.in](mailto:anaik@iisc.ac.in)

## Data Availability

All data are available upon reasonable request.

## Acknowledgments

We acknowledge funding support from the MoE, MeitY, and DST Nano Mission through NNetRA.

MPS acknowledges the INSPIRE Fellowship.

## References

- (1) Wang, Q. H.; Kalantar-Zadeh, K.; Kis, A.; Coleman, J. N.; Strano, M. S. Electronics and Optoelectronics of Two-Dimensional Transition Metal Dichalcogenides. *Nat. Nanotechnol.* **2012**, *7* (11), 699–712. <https://doi.org/10.1038/nnano.2012.193>.
- (2) Jariwala, D.; Sangwan, V. K.; Lauhon, L. J.; Marks, T. J.; Hersam, M. C. Emerging Device Applications for Semiconducting Two-Dimensional Transition Metal Dichalcogenides. *ACS Nano* **2014**, *8* (2), 1102–1120. <https://doi.org/10.1021/nn500064s>.
- (3) Ryder, C. R.; Wood, J. D.; Wells, S. A.; Hersam, M. C. Chemically Tailoring Semiconducting Two-Dimensional Transition Metal Dichalcogenides and Black Phosphorus. *ACS Nano* **2016**, *10* (4), 3900–3917. <https://doi.org/10.1021/acsnano.6b01091>.

- (4) Choi, W.; Choudhary, N.; Han, G. H.; Park, J.; Akinwande, D.; Lee, Y. H. Recent Development of Two-Dimensional Transition Metal Dichalcogenides and Their Applications. *Mater. Today* **2017**, *20* (3), 116–130. <https://doi.org/10.1016/j.mattod.2016.10.002>.
- (5) Conley, H. J.; Wang, B.; Ziegler, J. I.; Haglund, R. F. Jr.; Pantelides, S. T.; Bolotin, K. I. Bandgap Engineering of Strained Monolayer and Bilayer MoS<sub>2</sub>. *Nano Lett.* **2013**, *13* (8), 3626–3630. <https://doi.org/10.1021/nl4014748>.
- (6) Lee, G.-H.; Yu, Y.-J.; Cui, X.; Petrone, N.; Lee, C.-H.; Choi, M. S.; Lee, D.-Y.; Lee, C.; Yoo, W. J.; Watanabe, K.; Taniguchi, T.; Nuckolls, C.; Kim, P.; Hone, J. Flexible and Transparent MoS<sub>2</sub> Field-Effect Transistors on Hexagonal Boron Nitride-Graphene Heterostructures. *ACS Nano* **2013**, *7* (9), 7931–7936. <https://doi.org/10.1021/nn402954e>.
- (7) Wu, W.; Wang, L.; Li, Y.; Zhang, F.; Lin, L.; Niu, S.; Chenet, D.; Zhang, X.; Hao, Y.; Heinz, T. F.; Hone, J.; Wang, Z. L. Piezoelectricity of Single-Atomic-Layer MoS<sub>2</sub> for Energy Conversion and Piezotronics. *Nature* **2014**, *514* (7523), 470–474. <https://doi.org/10.1038/nature13792>.
- (8) Suzuki, H.; Liu, Y.; Misawa, M.; Nakano, C.; Wang, Y.; Nakano, R.; Ishimura, K.; Tsuruta, K.; Hayashi, Y. Intermediate State between MoSe<sub>2</sub> and Janus MoSeS during Atomic Substitution Process. *Nano Lett.* **2023**, *23* (10), 4533–4540. <https://doi.org/10.1021/acs.nanolett.3c00972>.
- (9) Ross, J. S.; Klement, P.; Jones, A. M.; Ghimire, N. J.; Yan, J.; Mandrus, D. G.; Taniguchi, T.; Watanabe, K.; Kitamura, K.; Yao, W.; Cobden, D. H.; Xu, X. Electrically Tunable Excitonic Light-Emitting Diodes Based on Monolayer WSe<sub>2</sub> p–n Junctions. *Nat. Nanotechnol.* **2014**, *9* (4), 268–272. <https://doi.org/10.1038/nnano.2014.26>.
- (10) Jones, A. M.; Yu, H.; Ghimire, N. J.; Wu, S.; Aivazian, G.; Ross, J. S.; Zhao, B.; Yan, J.; Mandrus, D. G.; Xiao, D.; Yao, W.; Xu, X. Optical Generation of Excitonic Valley Coherence in Monolayer WSe<sub>2</sub>. *Nat. Nanotechnol.* **2013**, *8* (9), 634–638. <https://doi.org/10.1038/nnano.2013.151>.
- (11) Tongay, S.; Sahin, H.; Ko, C.; Luce, A.; Fan, W.; Liu, K.; Zhou, J.; Huang, Y.-S.; Ho, C.-H.; Yan, J.; Ogletree, D. F.; Aloni, S.; Ji, J.; Li, S.; Li, J.; Peeters, F. M.; Wu, J. Monolayer Behaviour in Bulk ReS<sub>2</sub> Due to Electronic and Vibrational Decoupling. *Nat. Commun.* **2014**, *5* (1), 3252. <https://doi.org/10.1038/ncomms4252>.
- (12) Feng, Y.; Zhou, W.; Wang, Y.; Zhou, J.; Liu, E.; Fu, Y.; Ni, Z.; Wu, X.; Yuan, H.; Miao, F.; Wang, B.; Wan, X.; Xing, D. Raman Vibrational Spectra of Bulk to Monolayer ReS<sub>2</sub> with Lower Symmetry. *Phys. Rev. B* **2015**, *92* (5), 054110. <https://doi.org/10.1103/PhysRevB.92.054110>.
- (13) Jariwala, B.; Voiry, D.; Jindal, A.; Chalke, B. A.; Bapat, R.; Thamizhavel, A.; Chhowalla, M.; Deshmukh, M.; Bhattacharya, A. Synthesis and Characterization of ReS<sub>2</sub> and ReSe<sub>2</sub> Layered Chalcogenide Single Crystals. *Chem. Mater.* **2016**, *28* (10), 3352–3359. <https://doi.org/10.1021/acs.chemmater.6b00364>.
- (14) Zhou, Y.; Maity, N.; Rai, A.; Juneja, R.; Meng, X.; Roy, A.; Zhang, Y.; Xu, X.; Lin, J.-F.; Banerjee, S. K.; Singh, A. K.; Wang, Y. Stacking-Order-Driven Optical Properties and Carrier Dynamics in ReS<sub>2</sub>. *Adv. Mater.* **2020**, *32* (22), 1908311. <https://doi.org/10.1002/adma.201908311>.
- (15) Zhou, Y.; Maity, N.; Lin, J.-F.; Singh, A. K.; Wang, Y. Nonlinear Optical Absorption of ReS<sub>2</sub> Driven by Stacking Order. *ACS Photonics* **2021**, *8* (2), 405–411. <https://doi.org/10.1021/acsp Photonics.0c01225>.
- (16) He, R.; Yan, J.-A.; Yin, Z.; Ye, Z.; Ye, G.; Cheng, J.; Li, J.; Lui, C. H. Coupling and Stacking Order of ReS<sub>2</sub> Atomic Layers Revealed by Ultralow-Frequency Raman Spectroscopy. *Nano Lett.* **2016**, *16* (2), 1404–1409. <https://doi.org/10.1021/acs.nanolett.5b04925>.

- (17) Wang, J.; Zhou, Y. J.; Xiang, D.; Ng, S. J.; Watanabe, K.; Taniguchi, T.; Eda, G. Polarized Light-Emitting Diodes Based on Anisotropic Excitons in Few-Layer ReS<sub>2</sub>. *Adv. Mater.* **2020**, *32* (32), 2001890. <https://doi.org/10.1002/adma.202001890>.
- (18) Chenet, D. A.; Aslan, B.; Huang, P. Y.; Fan, C.; van der Zande, A. M.; Heinz, T. F.; Hone, J. C. In-Plane Anisotropy in Mono- and Few-Layer ReS<sub>2</sub> Probed by Raman Spectroscopy and Scanning Transmission Electron Microscopy. *Nano Lett.* **2015**, *15* (9), 5667–5672. <https://doi.org/10.1021/acs.nanolett.5b00910>.
- (19) Ho, C.-H. Dichroic Electro-Optical Behavior of Rhenium Sulfide Layered Crystal. *Cryst. Struct. Theory Appl.* **2013**, *2* (2), 65–69. <https://doi.org/10.4236/csta.2013.22009>.
- (20) Liu, E.; Fu, Y.; Wang, Y.; Feng, Y.; Liu, H.; Wan, X.; Zhou, W.; Wang, B.; Shao, L.; Ho, C.-H.; Huang, Y.-S.; Cao, Z.; Wang, L.; Li, A.; Zeng, J.; Song, F.; Wang, X.; Shi, Y.; Yuan, H.; Hwang, H. Y.; Cui, Y.; Miao, F.; Xing, D. Integrated Digital Inverters Based on Two-Dimensional Anisotropic ReS<sub>2</sub> Field-Effect Transistors. *Nat. Commun.* **2015**, *6* (1), 6991. <https://doi.org/10.1038/ncomms7991>.
- (21) Lin, Y.-C.; Komsa, H.-P.; Yeh, C.-H.; Björkman, T.; Liang, Z.-Y.; Ho, C.-H.; Huang, Y.-S.; Chiu, P.-W.; Krasheninnikov, A. V.; Suenaga, K. Single-Layer ReS<sub>2</sub>: Two-Dimensional Semiconductor with Tunable In-Plane Anisotropy. *ACS Nano* **2015**, *9* (11), 11249–11257. <https://doi.org/10.1021/acs.nano.5b04851>.
- (22) Chen, Y.; Peng, B.; Cong, C.; Shang, J.; Wu, L.; Yang, W.; Zhou, J.; Yu, P.; Zhang, H.; Wang, Y.; Zou, C.; Zhang, J.; Liu, S.; Xiong, Q.; Shao, H.; Liu, Z.; Zhang, H.; Huang, W.; Yu, T. In-Plane Anisotropic Thermal Conductivity of Few-Layered Transition Metal Dichalcogenide Td-WTe<sub>2</sub>. *Adv. Mater.* **2019**, *31* (7), 1804979. <https://doi.org/10.1002/adma.201804979>.
- (23) Luo, Z.; Maassen, J.; Deng, Y.; Du, Y.; Garrelts, R. P.; Lundstrom, M. S.; Ye, P. D.; Xu, X. Anisotropic In-Plane Thermal Conductivity Observed in Few-Layer Black Phosphorus. *Nat. Commun.* **2015**, *6* (1), 8572. <https://doi.org/10.1038/ncomms9572>.
- (24) Jang, H.; Ryder, C. R.; Wood, J. D.; Hersam, M. C.; Cahill, D. G. 3D Anisotropic Thermal Conductivity of Exfoliated Rhenium Disulfide. *Adv. Mater.* **2017**, *29* (35), 1700650. <https://doi.org/10.1002/adma.201700650>.
- (25) Tahbaz, S.; Pisana, S. Extreme In-Plane Thermal Conductivity Anisotropy in Rhenium-Based Dichalcogenides. *J. Phys. Mater.* **2024**, *7* (1), 015014. <https://doi.org/10.1088/2515-7639/ad1d8b>.
- (26) Castellanos-Gomez, A.; Buscema, M.; Molenaar, R.; Singh, V.; Janssen, L.; Zant, H. S. J. van der; Steele, G. A. Deterministic Transfer of Two-Dimensional Materials by All-Dry Viscoelastic Stamping. *2D Mater.* **2014**, *1* (1), 011002. <https://doi.org/10.1088/2053-1583/1/1/011002>.
- (27) Tsoukleri, G.; Parthenios, J.; Galiotis, C.; Papagelis, K. Embedded Trilayer Graphene Flakes under Tensile and Compressive Loading. *2D Mater.* **2015**, *2* (2), 024009. <https://doi.org/10.1088/2053-1583/2/2/024009>.
- (28) Huangfu, Z.; Wang, J.; Cheng, X.; Feng, S.; Liang, Y.; Yuan, C.; Zhu, X.; Wang, Z.; Zhang, H.; Yang, K. The Effect of Different Strain on the Structural and Optical Properties of Multilayer  $\gamma$ -InSe. *J. Alloys Compd.* **2023**, *961*, 170998. <https://doi.org/10.1016/j.jallcom.2023.170998>.
- (29) Dong, J.; Liu, S.; Fu, Y.; Wang, Q. Investigation of Strain-Induced Modulation on Electronic Properties of Graphene Field Effect Transistor. *Phys. Lett. A* **2017**, *381* (4), 292–297. <https://doi.org/10.1016/j.physleta.2016.11.003>.

- (30) Singh, M. P.; Dalal, R.; Singh, A.; Naik, A. Enhancement of Raman and Photoluminescence Intensity of Monolayer MoS<sub>2</sub> Using Engineered Substrates via Grayscale Electron-Beam Lithography. *ACS Appl. Nano Mater.* **2025**, *8* (5), 2171–2178. <https://doi.org/10.1021/acsnm.4c05513>.
- (31) Mak, K. F.; Lee, C.; Hone, J.; Shan, J.; Heinz, T. F. Atomically Thin MoS<sub>2</sub>: A New Direct-Gap Semiconductor. *Phys. Rev. Lett.* **2010**, *105* (13), 136805. <https://doi.org/10.1103/PhysRevLett.105.136805>.
- (32) Qiao, X.-F.; Wu, J.-B.; Zhou, L.; Qiao, J.; Shi, W.; Chen, T.; Zhang, X.; Zhang, J.; Ji, W.; Tan, P.-H. Polytypism and Unexpected Strong Interlayer Coupling in Two-Dimensional Layered ReS<sub>2</sub>. *Nanoscale* **2016**, *8* (15), 8324–8332. <https://doi.org/10.1039/C6NR01569G>.
- (33) Hart, L.; Dale, S.; Hoye, S.; Webb, J. L.; Wolverson, D. Rhenium Dichalcogenides: Layered Semiconductors with Two Vertical Orientations. *Nano Lett.* **2016**, *16* (2), 1381–1386. <https://doi.org/10.1021/acs.nanolett.5b04838>.
- (34) Balandin, A. A.; Ghosh, S.; Bao, W.; Calizo, I.; Teweldebrhan, D.; Miao, F.; Lau, C. N. Superior Thermal Conductivity of Single-Layer Graphene. *Nano Lett.* **2008**, *8* (3), 902–907. <https://doi.org/10.1021/nl0731872>.
- (35) Sahoo, S.; Gaur, A. P. S.; Ahmadi, M.; Guinel, M. J.-F.; Katiyar, R. S. Temperature-Dependent Raman Studies and Thermal Conductivity of Few-Layer MoS<sub>2</sub>. *J. Phys. Chem. C* **2013**, *117* (17), 9042–9047. <https://doi.org/10.1021/jp402509w>.
- (36) Yin, S.; Zhang, W.; Tan, C.; Chen, L.; Chen, J.; Li, G.; Zhang, H.; Zhang, Y.; Wang, W.; Li, L. Thermal Conductivity of Few-Layer PtS<sub>2</sub> and PtSe<sub>2</sub> Obtained from Optothermal Raman Spectroscopy. *J. Phys. Chem. C* **2021**, *125* (29), 16129–16135. <https://doi.org/10.1021/acs.jpcc.1c02522>.
- (37) He, C.; Xu, C.; Chen, C.; Tong, J.; Zhou, T.; Sun, S.; Liu, Z.; Cheng, H.-M.; Ren, W. Unusually High Thermal Conductivity in Suspended Monolayer MoSi<sub>2</sub>N<sub>4</sub>. *Nat. Commun.* **2024**, *15* (1), 4832. <https://doi.org/10.1038/s41467-024-48888-9>.
- (38) Kargar, F.; Coleman, E. A.; Ghosh, S.; Lee, J.; Gomez, M. J.; Liu, Y.; Magana, A. S.; Barani, Z.; Mohammadzadeh, A.; Debnath, B.; Wilson, R. B.; Lake, R. K.; Balandin, A. A. Phonon and Thermal Properties of Quasi-Two-Dimensional FePS<sub>3</sub> and MnPS<sub>3</sub> Antiferromagnetic Semiconductors. *ACS Nano* **2020**, *14* (2), 2424–2435. <https://doi.org/10.1021/acsnano.9b09839>.
- (39) Singh, M. P.; Mandal, M.; Sethupathi, K.; Rao, M. S. R.; Nayak, P. K. Study of Thermometry in Two-Dimensional Sb<sub>2</sub>Te<sub>3</sub> from Temperature-Dependent Raman Spectroscopy. *Nanoscale Res. Lett.* **2021**, *16* (1), 22. <https://doi.org/10.1186/s11671-020-03463-1>.
- (40) Luo, S.; Qi, X.; Yao, H.; Ren, X.; Chen, Q.; Zhong, J. Temperature-Dependent Raman Responses of the Vapor-Deposited Tin Selenide Ultrathin Flakes. *J. Phys. Chem. C* **2017**, *121* (8), 4674–4679. <https://doi.org/10.1021/acs.jpcc.6b12059>.
- (41) Yuan, P.; Wang, R.; Wang, T.; Wang, X.; Xie, Y. Nonmonotonic Thickness-Dependence of in-Plane Thermal Conductivity of Few-Layered MoS<sub>2</sub>: 2.4 to 37.8 Nm. *Phys. Chem. Chem. Phys.* **2018**, *20* (40), 25752–25761. <https://doi.org/10.1039/C8CP02858C>.
- (42) Gu, X.; Li, B.; Yang, R. Layer Thickness-Dependent Phonon Properties and Thermal Conductivity of MoS<sub>2</sub>. *J. Appl. Phys.* **2016**, *119* (8), 085106. <https://doi.org/10.1063/1.4942827>.
- (43) Cai, Q.; Scullion, D.; Gan, W.; Falin, A.; Zhang, S.; Watanabe, K.; Taniguchi, T.; Chen, Y.; Santos, E. J. G.; Li, L. H. High Thermal Conductivity of High-Quality Monolayer Boron Nitride and Its Thermal Expansion. *Sci. Adv.* **2019**, *5* (6), eaav0129. <https://doi.org/10.1126/sciadv.aav0129>.

(44) Easy, E.; Gao, Y.; Wang, Y.; Yan, D.; Goushehgir, S. M.; Yang, E.-H.; Xu, B.; Zhang, X. Experimental and Computational Investigation of Layer-Dependent Thermal Conductivities and Interfacial Thermal Conductance of One- to Three-Layer WSe<sub>2</sub>. *ACS Appl. Mater. Interfaces* **2021**, *13* (11), 13063–13071. <https://doi.org/10.1021/acsami.0c21045>.

## Supporting Information

### Anisotropic In-plane Thermal Conductivity of Freestanding Few-layer ReS<sub>2</sub>

Manavendra Pratap Singh<sup>1</sup>, Akshay Naik<sup>1\*</sup>

<sup>1</sup>Centre for Nanoscience and Engineering, Indian Institute of Science,

Bengaluru, Karnataka 560012, India

\*Corresponding author: [anaik@iisc.ac.in](mailto:anaik@iisc.ac.in)

**S1. Fabrication of the holey substrate**

**S2. The extended Raman spectra ~3.5 nm thick of ReS<sub>2</sub>**

**S3. Stacking order, AA confirmation of ~3.5 nm thick ReS<sub>2</sub> sample by Raman spectra**

**S4. Comparison of the power-dependent Raman spectra on the substrate-supported and freestanding ReS<sub>2</sub>**

**S5. Laser power and temperature-dependent Raman spectra of mode III for ~3.5 nm thick ReS<sub>2</sub> sample (AA stacking)**

**S6. The optical image, Raman, and AFM characterization of ~3.5 nm ReS<sub>2</sub> (AB stacking)**

**S7. Laser power and temperature-dependent Raman spectra of mode V for ~3.5 nm thick ReS<sub>2</sub> sample (AB stacking)**

**S8. Laser power and temperature-dependent Raman spectra of mode III for ~3.5 nm thick ReS<sub>2</sub> sample (AB stacking)**

**S9. Optical images, AFM and Raman characterization of ~2.5, ~5.2, and ~8 nm ReS<sub>2</sub> samples**

**S10. Laser power and temperature-dependent Raman spectra of modes III and V for ~2.5 nm (AA), ~5.2 nm (AA), and ~8 nm (AB) ReS<sub>2</sub> samples**

**S11. Tabulation of the first-order power coefficients, temperature coefficients, and anisotropic in-plane thermal conductivities using mode V for all ReS<sub>2</sub> samples**

**S12. Tabulation of the first-order power coefficients, temperature coefficients, and anisotropic in-plane thermal conductivities using mode III for all ReS<sub>2</sub> samples**

### **S1. Fabrication of the holey substrate**

We use a highly p-doped Si wafer with ~290 nm thick thermally grown SiO<sub>2</sub>/Si. We cut a 4-inch wafer into small rectangular pieces and then cleaned these small pieces. We dip these small pieces of SiO<sub>2</sub>/Si chips into acetone and ultrasonicate it for 3 minutes. Then, these chips are transferred into iso-propyl-alcohol (IPA) and are again sonicated for 3 minutes. We carry out standard optical lithography throughout the work using Mask writer Heidelberg (uPG501). We use AZ5214E positive optical resist. At first, we spin-coated AZ5214E uniformly on the substrate at a rotating speed of 4000 rpm for 40 seconds (including 5 seconds of ramp time). Then, the substrate is heated at 110 °C for 60 seconds on a hot plate to remove the solvent from the resist film. 10×10 arrays of circles (diameter ~4 μm) have been directly written by Mask writer Heidelberg (uPG501) with defocus -2 and exposure time 90 ms. The sample is developed in AZ726MIF developer for 25 seconds and then placed in the DI water, which acts as a stopper. It is then dried out using a N<sub>2</sub> blow-drier. The sample was hard-baked for 3 min at 110 °C for dry etch processes. We successfully fabricated the arrays of holes with a depth of ~685 nm and diameter of ~4 μm followed by reactive ion etching (RIE) of SiO<sub>2</sub> & Si layers. The atomic force microscopy (AFM) image is attached below in Figure S1.

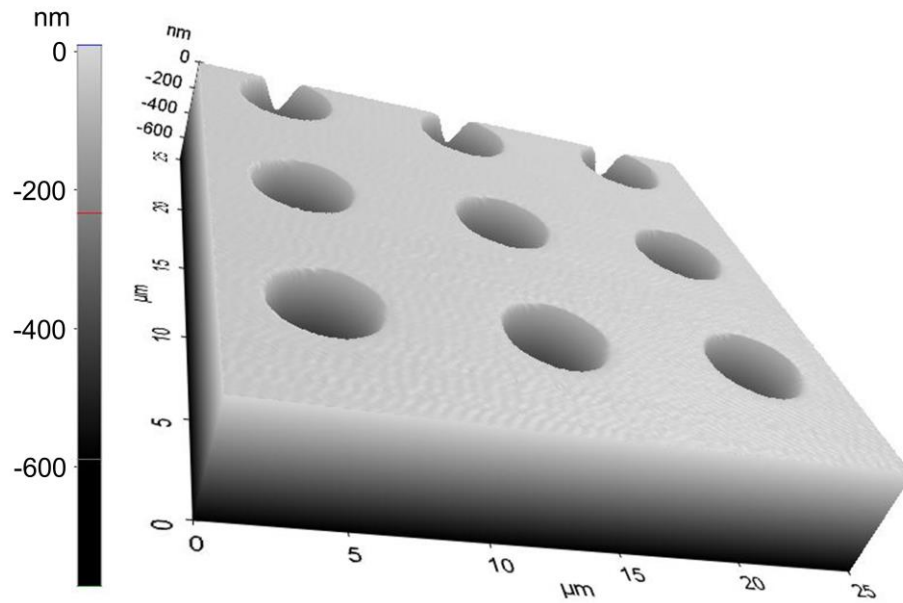


**Figure S1.** 3D AFM image of the holey substrate.

## S2. The extended Raman spectra $\sim 3.5$ nm thick of $\text{ReS}_2$

Figure S2 shows 18 Raman modes of  $\sim 3.5$  nm thick  $\text{ReS}_2$ , which were previously reported for  $\text{ReS}_2^1$ .

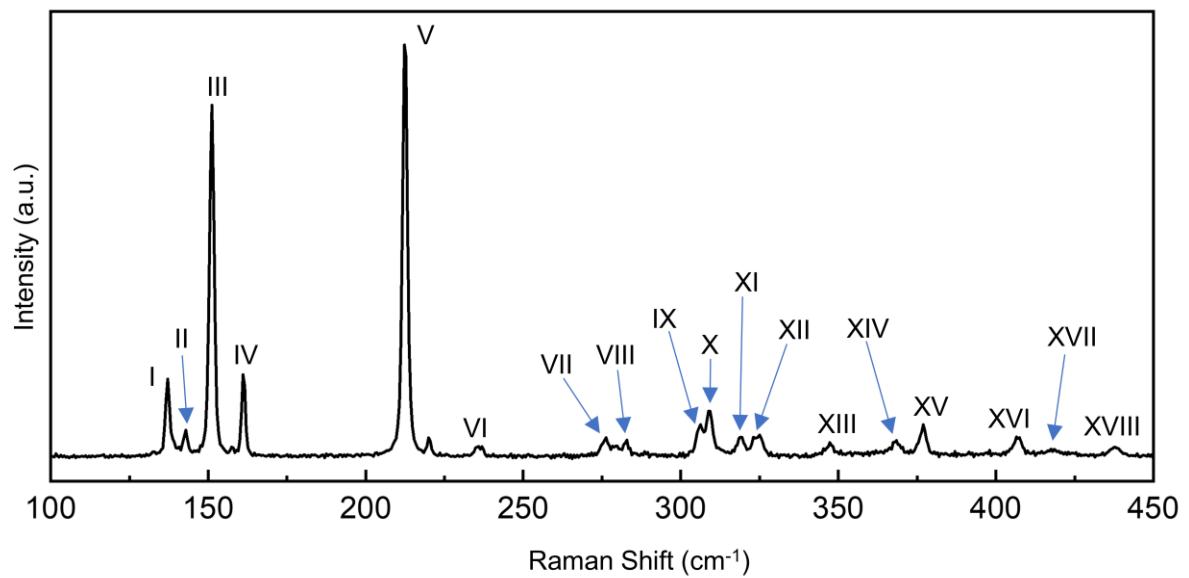


**Figure S2.** Raman spectra of  $\sim 3.5$  nm thick  $\text{ReS}_2$ .

### S3. Stacking order, AA confirmation of ~3.5 nm thick ReS<sub>2</sub> sample by Raman spectra

We use the separation between Raman modes I and III to identify whether the stacking order is AA or AB<sup>2-4</sup>. For monolayer ReS<sub>2</sub>, the peak separation was ~ 17 cm<sup>-1</sup>. The separation was less than that for AA stacking, and for AB stacking, it was more<sup>2,3</sup>. Figure S3 shows that the flake's separation between Raman modes III and I is 14.02 cm<sup>-1</sup>, which confirms the AA stacking order of ~3.5 nm thick ReS<sub>2</sub>.

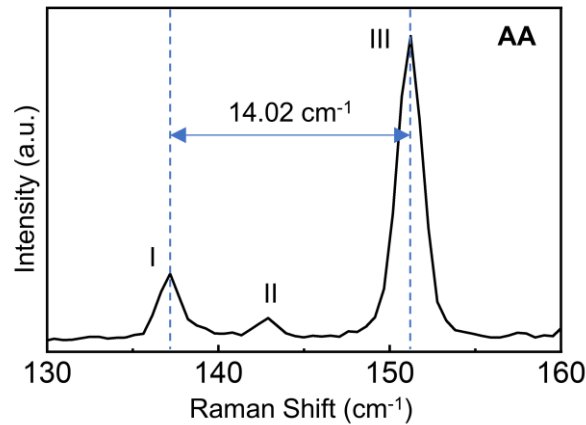


**Figure S3.** Raman spectra of AA stacking ReS<sub>2</sub> with thickness ~3.5 nm.

### S4. Comparison of the power-dependent Raman spectra on the substrate-supported and freestanding ReS<sub>2</sub>

Figures S4a and S4b show the power-dependent Raman spectra on the substrate-supported and freestanding ReS<sub>2</sub>. There is no substantial shift in the peak position of Raman modes on substrate-supported ReS<sub>2</sub> with laser power variation owing to faster heat dissipation through SiO<sub>2</sub>/Si<sup>5</sup>. However, the freestanding ReS<sub>2</sub> shows a significant red shift with increasing laser power, which is used in calculating thermal conductivity.

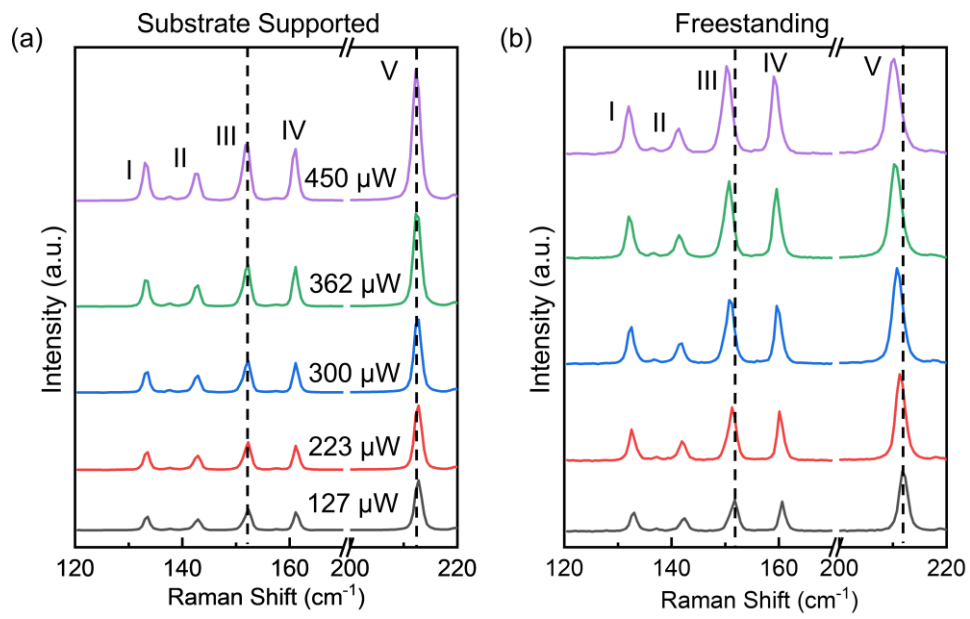


**Figure S4.** Power-dependent Raman spectra on (a) substrate supported and (b) freestanding  $\text{ReS}_2$ , respectively.

### S5. Laser power and temperature-dependent Raman spectra of mode III for ~3.5 nm thick ReS<sub>2</sub> sample (AA stacking)

The laser power and temperature-dependent Raman spectra of mode III for the ~3.5 nm freestanding ReS<sub>2</sub> (AA) along the *b*-axis and cross *b*-axis are shown in Figure S5a-b and Figure S5c-d. The accurate peak positions of the Raman modes were extracted by Voigt function fitting. The extracted first-order power coefficient of mode III is found to be  $-7.23 \pm 0.19 \text{ cm}^{-1}/\text{mW}$  along the *b*-axis and  $-5.87 \pm 0.36 \text{ cm}^{-1}/\text{mW}$  along the cross *b*-axis (Figure S5e). The extracted first-order temperature coefficients were  $\chi_{b, \text{mode III}} = -(0.76 \pm 0.02) \times 10^{-2} \text{ cm}^{-1}/\text{K}$  and  $\chi_{\perp b, \text{mode III}} = -(0.51 \pm 0.03) \times 10^{-2} \text{ cm}^{-1}/\text{K}$  (Figure S5e). Using the first-order temperature and power coefficients, the calculated thermal conductivities are  $48 \pm 3 \text{ W/m-K}$  (*b*-axis) and  $39 \pm 5 \text{ W/m-K}$  (cross *b*-axis) for the ~3.5 nm thick ReS<sub>2</sub> of AA stacking. Thermal conductivity calculated using mode III agrees with thermal conductivity calculated using mode V of the sample.

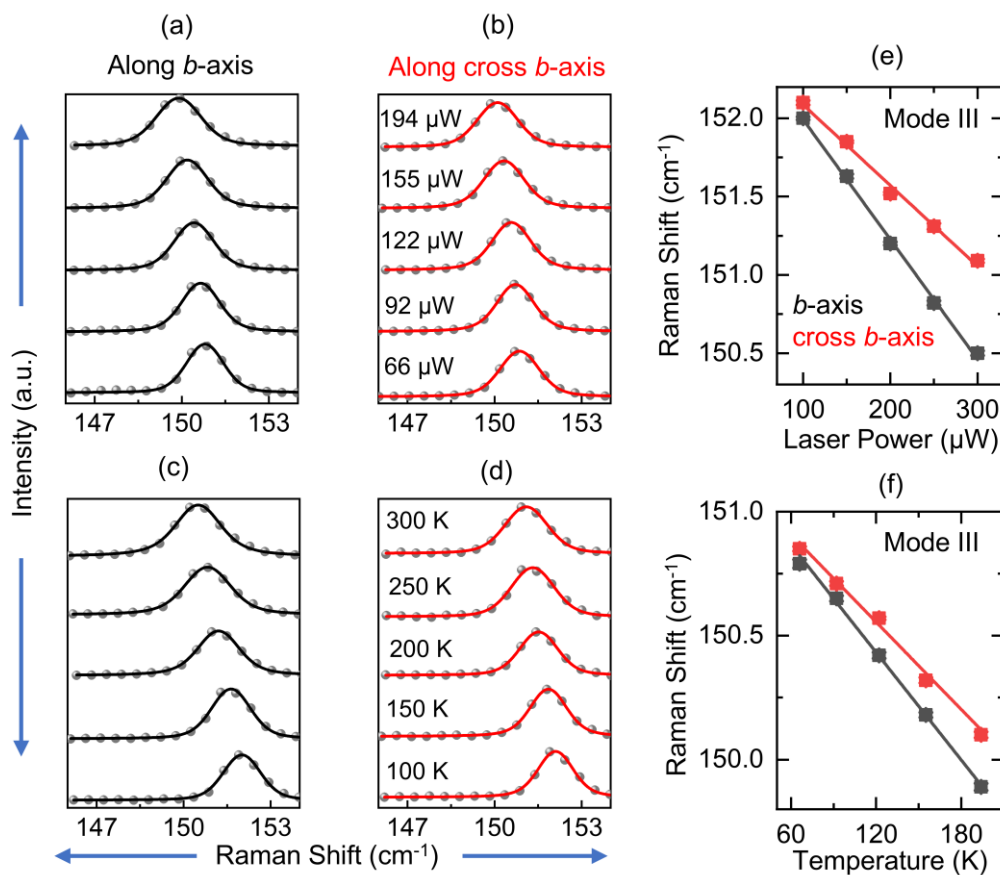


**Figure S5.** Power-dependent  $\mu$ -Raman spectra of mode III for  $\sim 3.5$  nm thick ReS<sub>2</sub> (AA) along the (a) *b*-axis and (b) cross *b*-axis. Temperature-dependent micro-Raman spectra of mode III of the same sample along (c) *b*-axis and (d) cross *b*-axis. (e) Raman peak position vs. laser power plot extracted from the Voigt function fitting of (a) and (b). The lines (red and black) are linear fitting to obtain the first-order power coefficient. (f) Raman peak position vs. laser power plot extracted from the Voigt function fitting of (c) and (d). The lines (red and black) are linear fitting to obtain the first-order temperature coefficient.

### **S6. The optical image, Raman, and AFM characterization of $\sim 3.5$ nm ReS<sub>2</sub> (AB stacking)**

Figure S6a shows that the separation between Raman modes III and I of the ReS<sub>2</sub> flake is  $18.52 \text{ cm}^{-1}$ , which confirms the AB stacking order of ReS<sub>2</sub>. Figure S6b shows an optical image of the ReS<sub>2</sub> flake on the "holey" substrate of SiO<sub>2</sub>/Si. The thickness ( $\sim 3.5$  nm) of the transferred flake was measured using atomic force microscopy (AFM) at the edge of the flake (Figure S6c). To find the *b*-axis, we performed angle-resolved polarized Raman measurements of the ReS<sub>2</sub> flake, similar to the previous sample. Figure S6d shows a polar plot of the Raman intensity of modes III and V of the ReS<sub>2</sub> flake (Figure S6d).

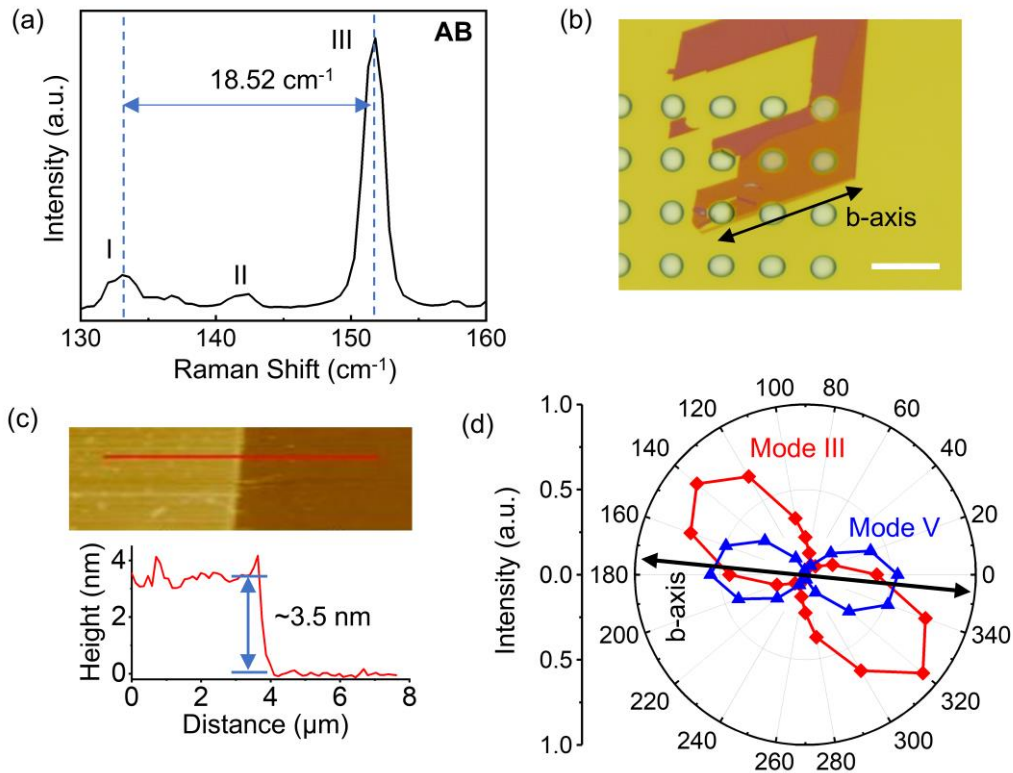


**Figure S6.** (a) Raman spectra of AB stacking ReS<sub>2</sub> with thickness ~3.5 nm. (b) Optical micrograph of the ReS<sub>2</sub> flake on the array of holes in SiO<sub>2</sub>/Si substrate. The flake has a sharp edge along the *b*-axis, which is denoted by a double-headed arrow (black). The scale bar is 10 μm. (c) AFM image of the sample's edge and height profile. (d) Polar plot of the Raman intensities of modes III (red) and V (blue).

### S7. Laser power and temperature-dependent Raman spectra of mode V for ~3.5 nm thick ReS<sub>2</sub> sample (AB stacking)

The laser power and temperature-dependent Raman spectra of mode V for the ~3.5 nm freestanding ReS<sub>2</sub> (AB stacking) along the *b*-axis and cross *b*-axis are shown in Figure S7a-b and Figure S7c-d, respectively. All Raman modes of the freestanding ReS<sub>2</sub> were redshifted with increasing laser power or temperature. The accurate peak positions of the Raman modes were extracted by Voigt function fitting.

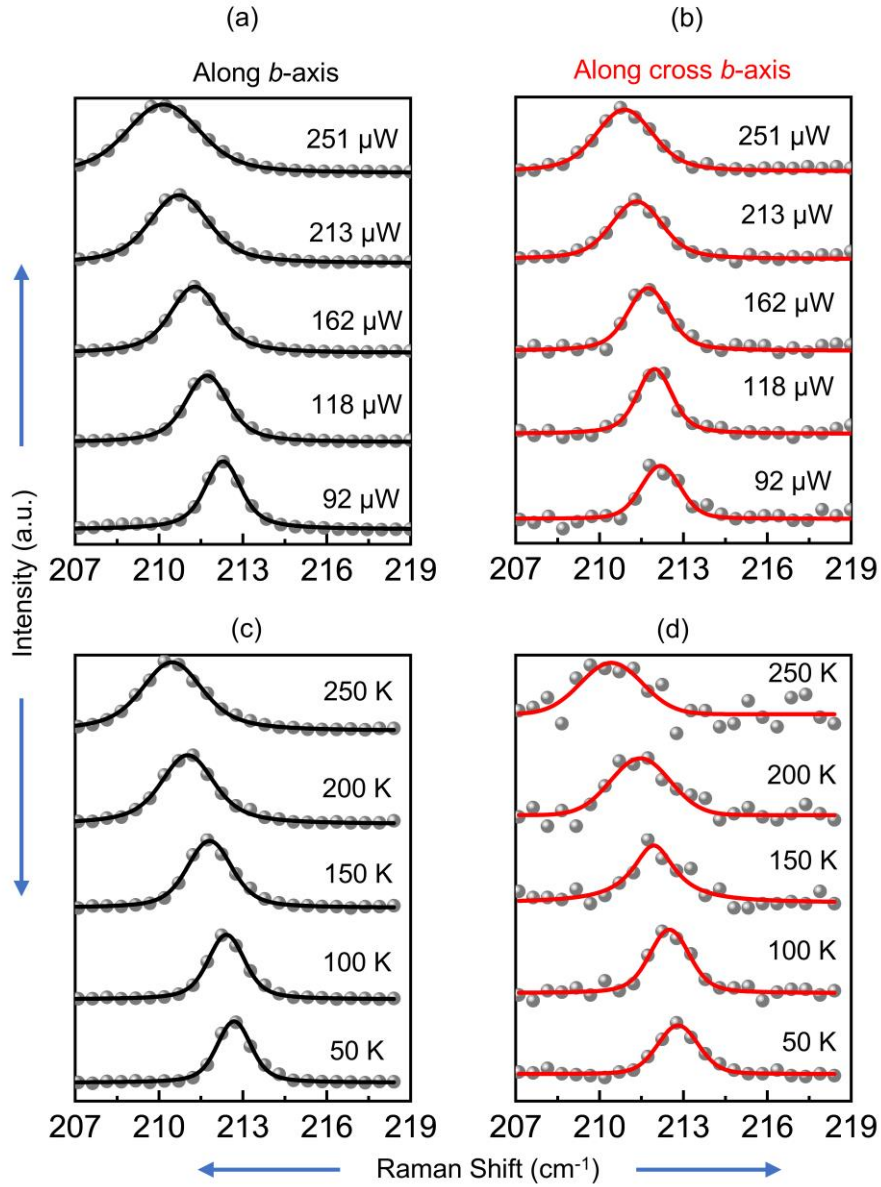


**Figure S7.** Power-dependent  $\mu$ -Raman spectra of mode V for  $\sim 3.5$  nm thick ReS<sub>2</sub> (AB) along the (a) b-axis and (b) cross b-axis. Temperature-dependent micro-Raman spectra of mode V of the same sample along (c) b-axis and (d) cross b-axis. All spectra were fitted with the Voigt function.

### S8. Laser power and temperature-dependent Raman spectra of mode III for $\sim 3.5$ nm thick ReS<sub>2</sub> sample (AB stacking)

The laser power and temperature-dependent Raman spectra of mode III for the  $\sim 3.5$  nm freestanding ReS<sub>2</sub> (AB) along the  $b$ -axis and cross  $b$ -axis are shown in Figure S8a-b and Figure S8c-d. The accurate peak positions of the Raman modes were extracted by Voigt function fitting. The extracted first-order power coefficient of mode III is found to be  $-8.67 \pm 0.33$  cm<sup>-1</sup>/mW along the  $b$ -axis and  $-5.98 \pm 0.22$  cm<sup>-1</sup>/mW along the cross  $b$ -axis (Figure S8e). The extracted temperature coefficients were  $\chi_{b, mode III} = -(0.8 \pm 0.02) \times 10^{-2}$  cm<sup>-1</sup>/K and  $\chi_{\perp b, mode III} = -(0.50 \pm 0.01) \times 10^{-2}$  cm<sup>-1</sup>/K (Figure S8f). Using the first-order temperature and power coefficients, the calculated thermal conductivities are  $42 \pm 3$  W/m-K ( $b$ -axis) and  $38 \pm 2$  W/m-K (cross  $b$ -axis) for the  $\sim 3.5$  nm thick ReS<sub>2</sub> of AB stacking. Thermal conductivity calculated using mode III agrees well with thermal conductivity calculated using mode V of the sample.

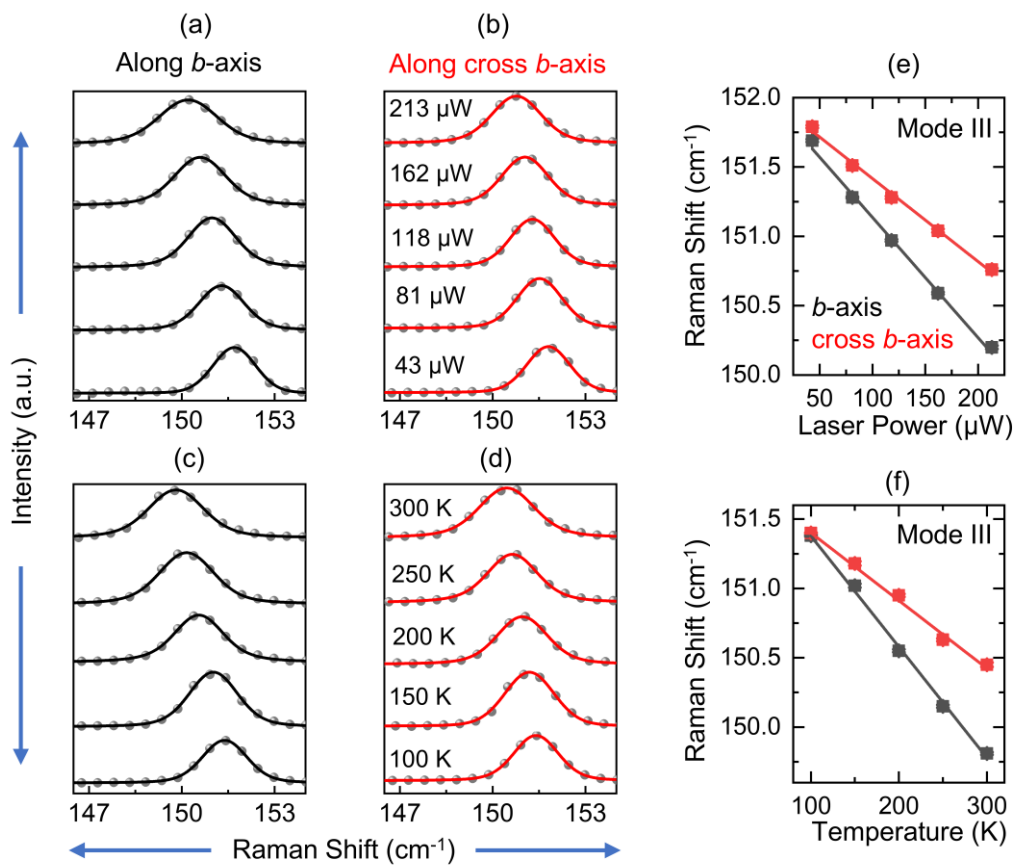


**Figure S8.** Power-dependent  $\mu$ -Raman spectra of mode III for  $\sim 3.5$  nm thick  $\text{ReS}_2$  (AB) along the (a) b-axis and (b) cross b-axis. Temperature-dependent micro-Raman spectra of mode III of the same sample along (c) b-axis and (d) cross b-axis. (e) Raman peak position vs. laser power plot extracted from the Voigt function fitting of (a) and (b). The lines (red and black) are linear fitting to obtain the first-order power coefficient. (f) Raman peak position vs. laser power plot extracted from the Voigt function fitting of (c) and (d). The lines (red and black) are linear fitting to obtain the first-order temperature coefficient.

### S9. Optical images, AFM and Raman characterization of $\sim 2.5$ , $\sim 5.2$ , and $\sim 8$ nm $\text{ReS}_2$ samples

Figure S9a-c shows optical micrographs of three different  $\text{ReS}_2$  flakes on the array of holes in the  $\text{SiO}_2/\text{Si}$  substrate. The b-axis is denoted by a double-headed arrow (black) on each optical image. Figure S9d-f shows their AFM images of the sample's edges and height profiles. The measured thicknesses are  $\sim 2.5$  nm,  $\sim 5.2$  nm, and  $\sim 8$  nm. Figure S9g-i shows the separation between Raman modes III and I of the  $\text{ReS}_2$  flakes. For  $\sim 2.5$  nm thick flake, the separation is  $14.89 \text{ cm}^{-1}$ , which confirms the AA stacking. The flake with thickness  $\sim 5.2$  nm shows the separation:  $13.26 \text{ cm}^{-1}$ , which confirms the AA stacking. For  $\sim 8$  nm thick flake, the separation is  $18.74 \text{ cm}^{-1}$ , which confirms the AB stacking.

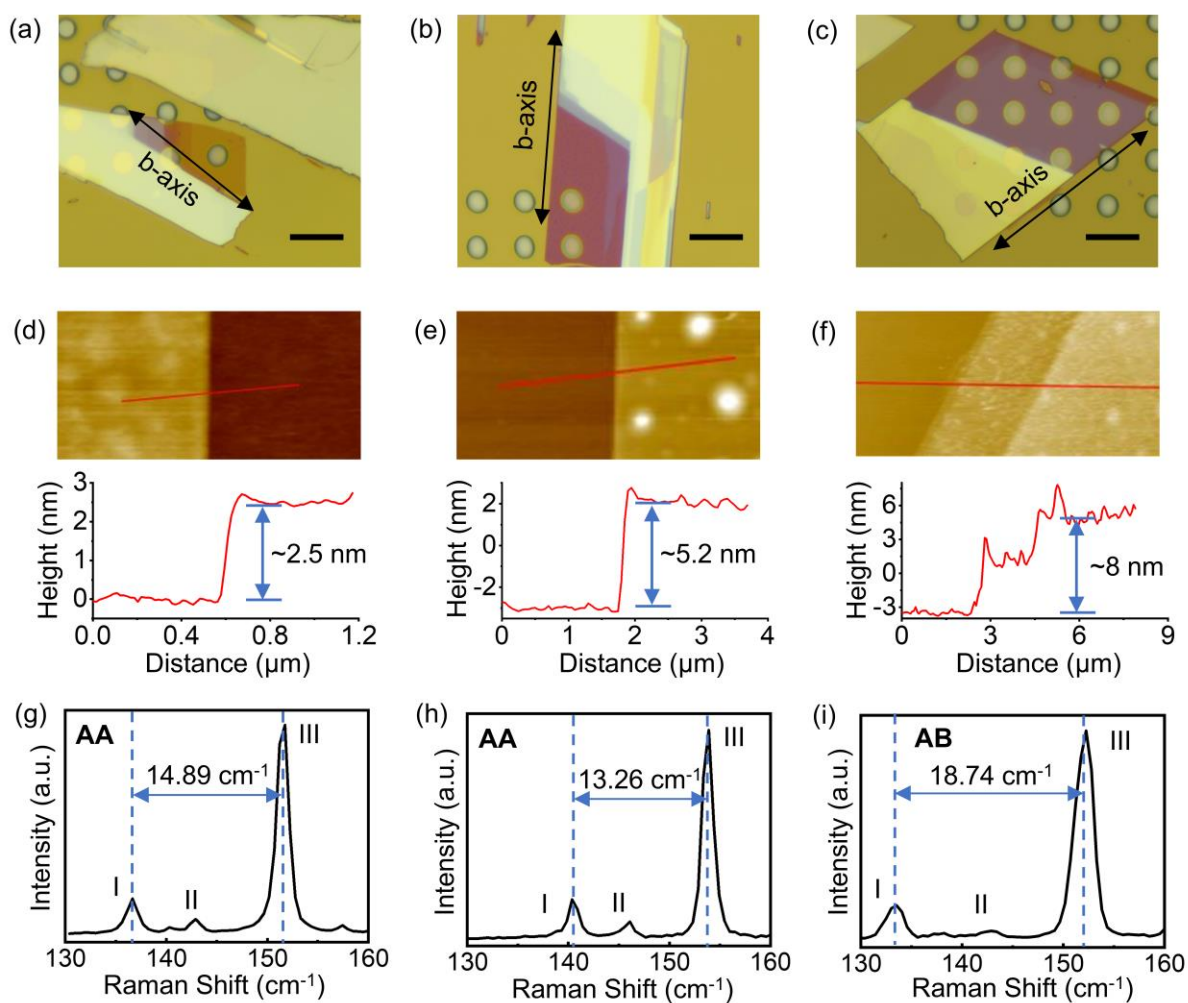


**Figure S9.** (a-c) Optical micrograph of the ReS<sub>2</sub> flake on the array of holes in SiO<sub>2</sub>/Si substrate. The b-axis is denoted by a double-headed arrow (black). The scale bar is 10 μm. (d-f) AFM image of the sample's edge and height profile. (g-i) Raman spectra of ReS<sub>2</sub> with thicknesses ~2.5 nm (AA stacking), ~5.2 nm (AA stacking), and ~8 nm (AB stacking), respectively.

**S10. Laser power and temperature-dependent Raman spectra of modes III and V for ~2.5 nm (AA), ~5.2 nm (AA), and ~8 nm (AB) ReS<sub>2</sub> samples**

**(A) Mode III of ~2.5 nm ReS<sub>2</sub> (AA)**

The extracted first-order power coefficient, temperature coefficient of mode III along the *b*-axis and cross *b*-axis, and the calculated anisotropic thermal conductivities are listed in Table S2.

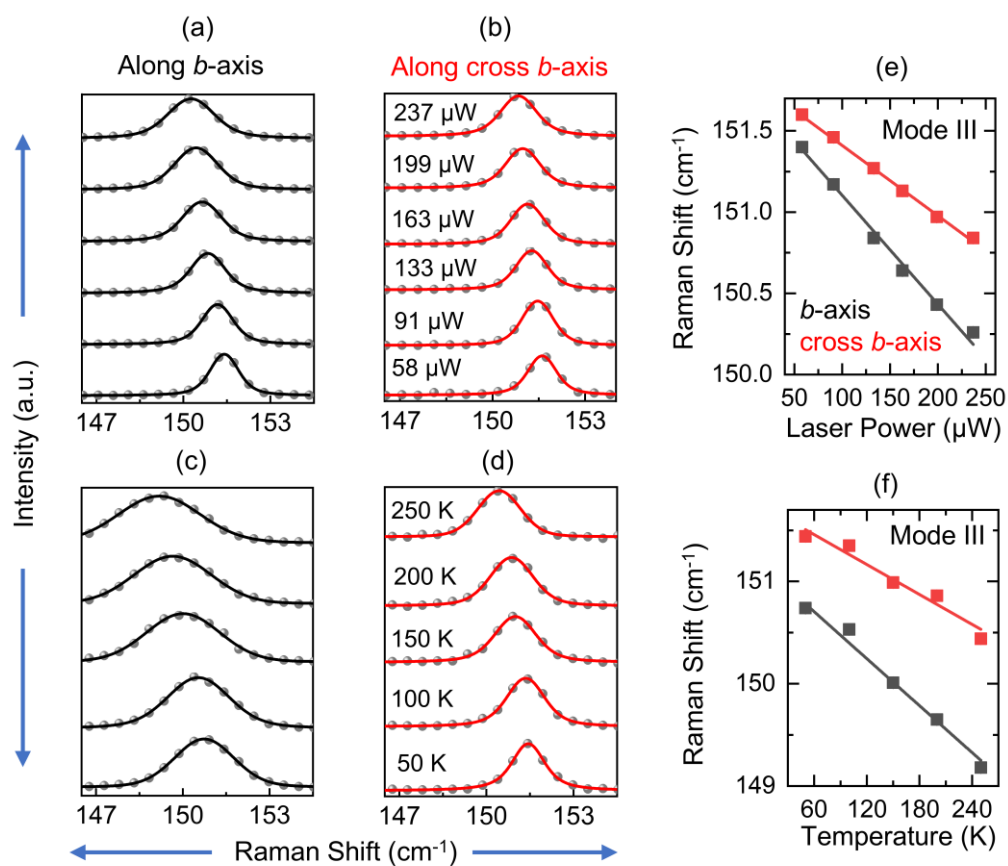


**Figure S10.** Power-dependent  $\mu$ -Raman spectra of mode III for ~2.5 nm thick ReS<sub>2</sub> (AA) along the (a) *b*-axis and (b) cross *b*-axis. Temperature-dependent micro-Raman spectra of mode III of the same sample along (c) *b*-axis and (d) cross *b*-axis. (e) Raman peak position vs. laser power plot extracted from the Voigt function fitting of (a) and (b). The lines (red and black) are linear fitting to obtain the first-order power coefficient. (f) Raman peak position vs. laser power plot extracted from the Voigt

function fitting of (c) and (d). The lines (red and black) are linear fitting to obtain the first-order temperature coefficient.

### (B) Mode V of $\sim 2.5$ nm ReS<sub>2</sub> (AA)

The extracted first-order power coefficient, temperature coefficient of mode V along the *b*-axis and cross *b*-axis, and the calculated anisotropic thermal conductivities are listed in Table S1.

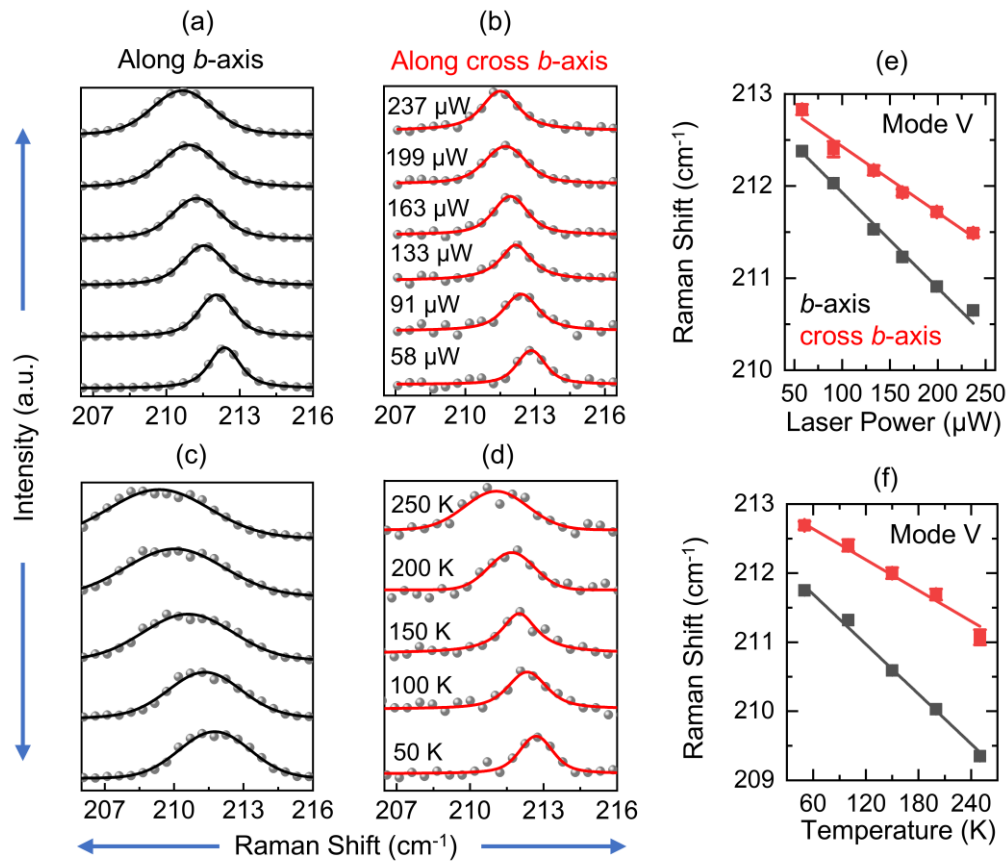


**Figure S11.** Power-dependent  $\mu$ -Raman spectra of mode V for  $\sim 2.5$  nm thick ReS<sub>2</sub> (AA) along the (a) *b*-axis and (b) cross *b*-axis. Temperature-dependent micro-Raman spectra of mode V of the same sample along (c) *b*-axis and (d) cross *b*-axis. (e) Raman peak position vs. laser power plot extracted from the Voigt function fitting of (a) and (b). The lines (red and black) are linear fitting to obtain the first-order power coefficient. (f) Raman peak position vs. laser power plot extracted from the Voigt function fitting of (c) and (d). The lines (red and black) are linear fitting to obtain the first-order temperature coefficient.

### (C) Mode III of $\sim 5.2$ nm $\text{ReS}_2$ (AA)

The extracted first-order power coefficient, temperature coefficient of mode III along the  $b$ -axis and cross  $b$ -axis, and the calculated anisotropic thermal conductivities are listed in Table S2.

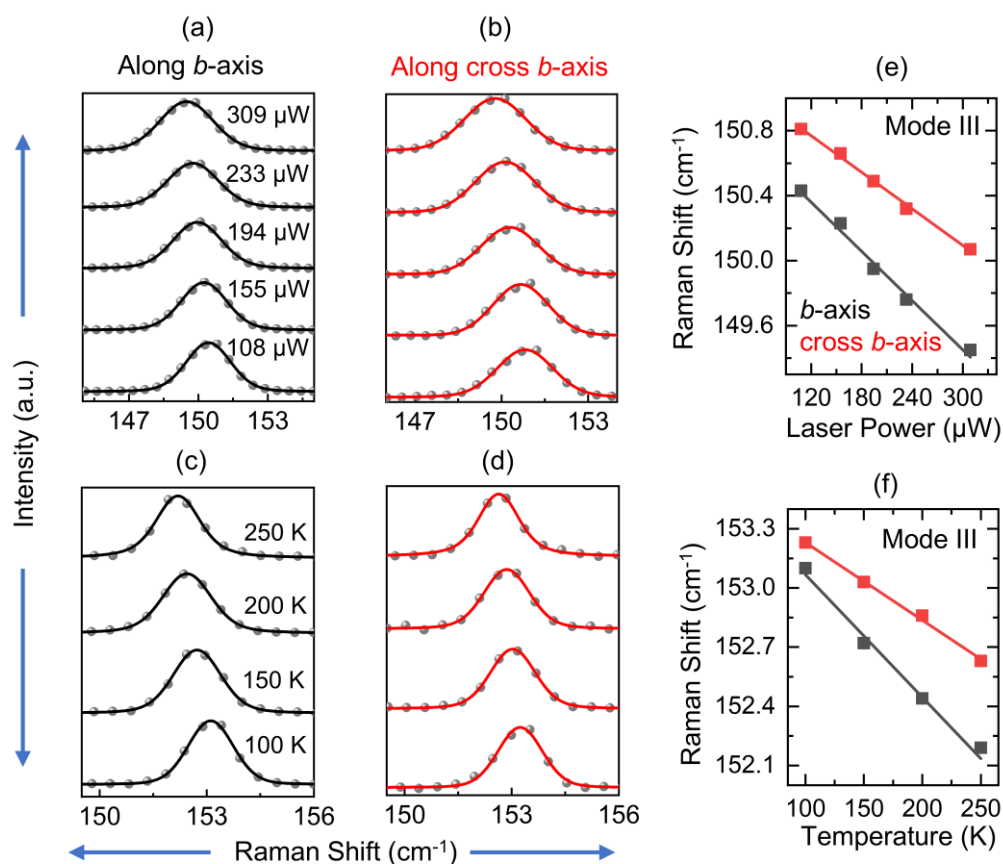


**Figure S12.** Power-dependent  $\mu$ -Raman spectra of mode III for  $\sim 5.2$  nm thick  $\text{ReS}_2$  (AA) along the (a)  $b$ -axis and (b) cross  $b$ -axis. Temperature-dependent micro-Raman spectra of mode III of the same sample along (c)  $b$ -axis and (d) cross  $b$ -axis. (e) Raman peak position vs. laser power plot extracted from the Voigt function fitting of (a) and (b). The lines (red and black) are linear fitting to obtain the first-order power coefficient. (f) Raman peak position vs. laser power plot extracted from the Voigt function fitting of (c) and (d). The lines (red and black) are linear fitting to obtain the first-order temperature coefficient.

### (D) Mode V of $\sim 5.2$ nm $\text{ReS}_2$ (AA)

The extracted first-order power coefficient, temperature coefficient of mode V along the  $b$ -axis and cross  $b$ -axis, and the calculated anisotropic thermal conductivities are listed in Table S1.

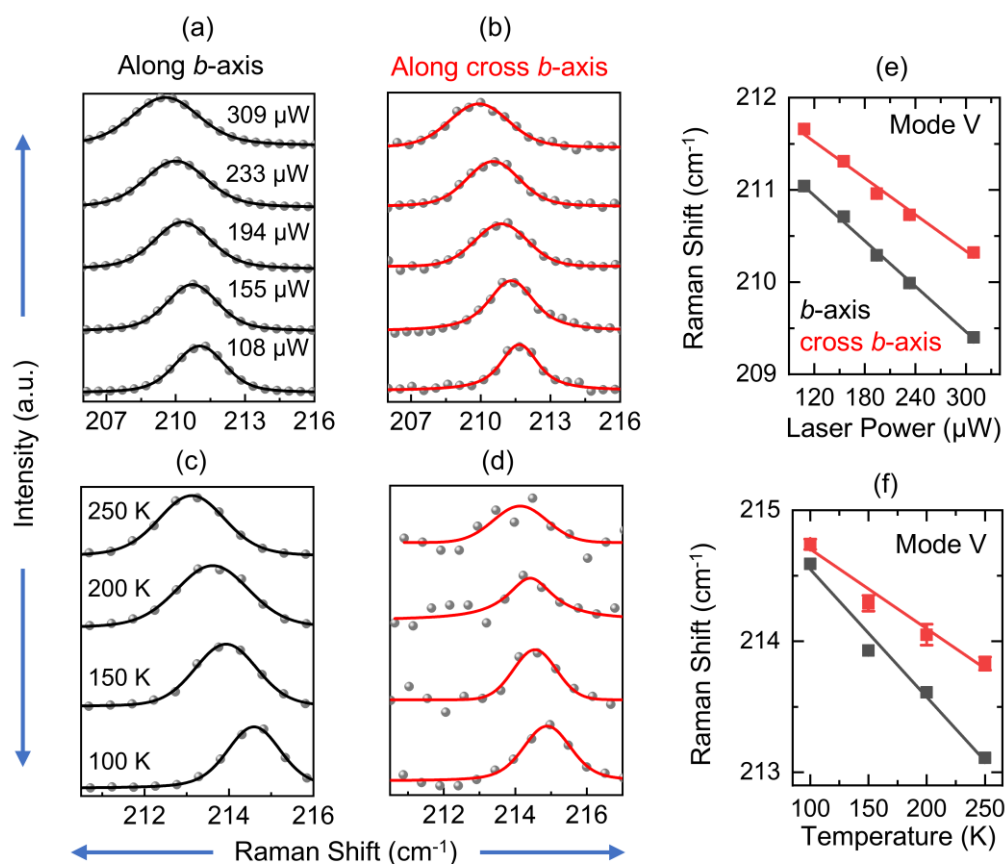


**Figure S13.** Power-dependent  $\mu$ -Raman spectra of mode V for  $\sim 5.2$  nm thick  $\text{ReS}_2$  (AA) along the (a)  $b$ -axis and (b) cross  $b$ -axis. Temperature-dependent micro-Raman spectra of mode V of the same sample along (c)  $b$ -axis and (d) cross  $b$ -axis. (e) Raman peak position vs. laser power plot extracted from the Voigt function fitting of (a) and (b). The lines (red and black) are linear fitting to obtain the first-order power coefficient. (f) Raman peak position vs. laser power plot extracted from the Voigt function fitting of (c) and (d). The lines (red and black) are linear fitting to obtain the first-order temperature coefficient.

### (E) Mode III of $\sim 8$ nm $\text{ReS}_2$ (AB)

The extracted first-order power and temperature coefficients of mode III along the  $b$ -axis and cross  $b$ -axis and the calculated anisotropic thermal conductivities are listed in Table S2.

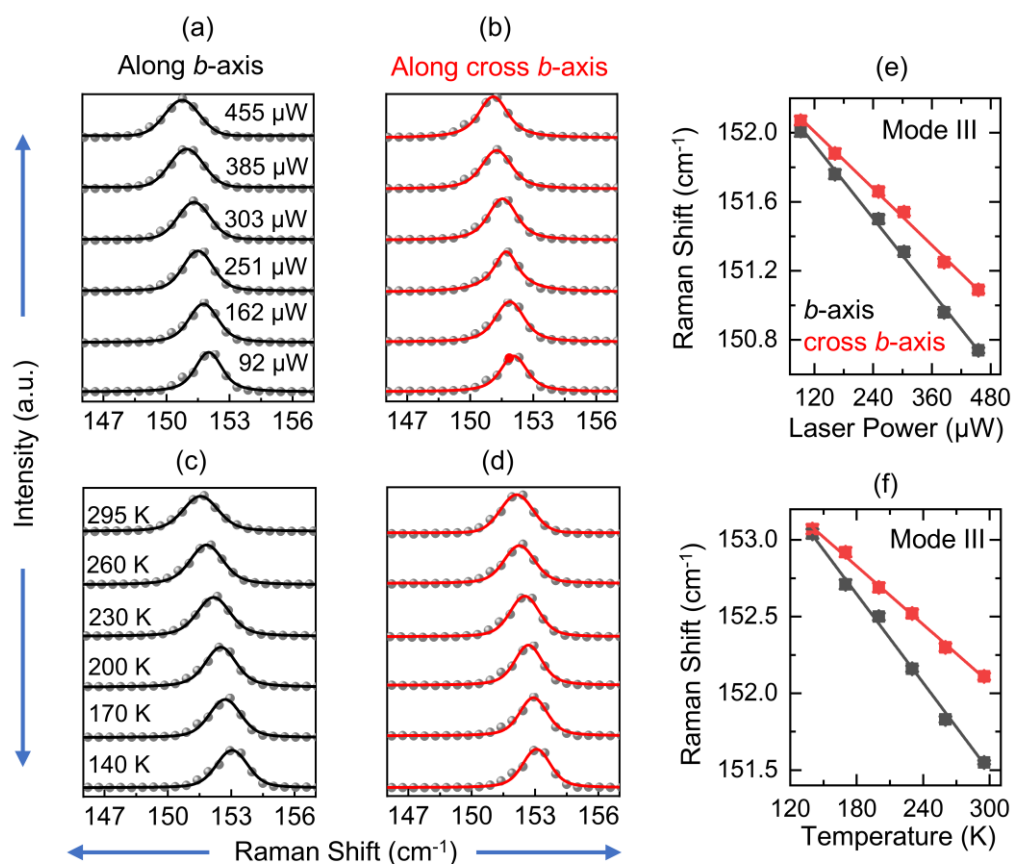


**Figure S14.** Power-dependent  $\mu$ -Raman spectra of mode III for  $\sim 8$  nm thick  $\text{ReS}_2$  (AA) along the (a)  $b$ -axis and (b) cross  $b$ -axis. Temperature-dependent micro-Raman spectra of mode III of the same sample along (c)  $b$ -axis and (d) cross  $b$ -axis. (e) Raman peak position vs. laser power plot extracted from the Voigt function fitting of (a) and (b). The lines (red and black) are linear fitting to obtain the first-order power coefficient. (f) Raman peak position vs. laser power plot extracted from the Voigt function fitting of (c) and (d). The lines (red and black) are linear fitting to obtain the first-order temperature coefficient.

### (F) Mode V of $\sim 8$ nm ReS<sub>2</sub> (AB)

The extracted first-order power coefficient, temperature coefficient of mode V along the  $b$ -axis and cross  $b$ -axis, and the calculated anisotropic thermal conductivities are listed in Table S1.

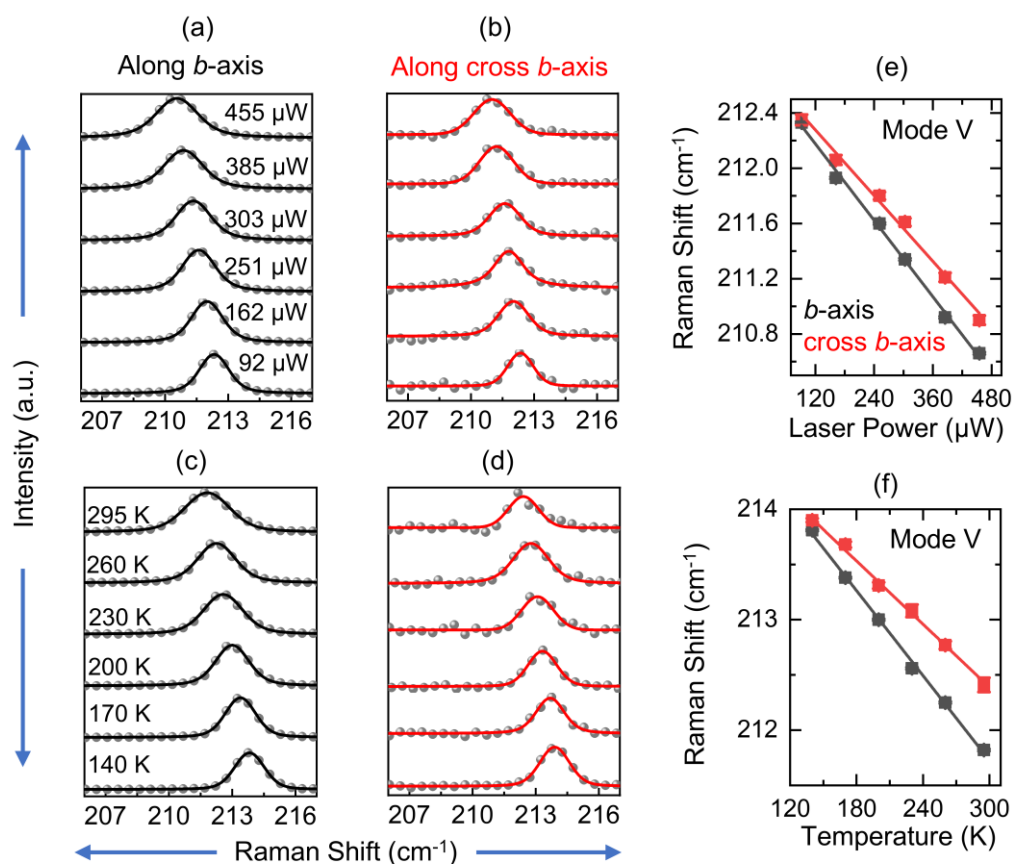


**Figure S15.** Power-dependent  $\mu$ -Raman spectra of mode V for  $\sim 8$  nm thick ReS<sub>2</sub> (AB) along the (a)  $b$ -axis and (b) cross  $b$ -axis. Temperature-dependent micro-Raman spectra of mode V of the same sample along (c)  $b$ -axis and (d) cross  $b$ -axis. (e) Raman peak position vs. laser power plot extracted from the Voigt function fitting of (a) and (b). The lines (red and black) are linear fitting to obtain the first-order power coefficient. (f) Raman peak position vs. laser power plot extracted from the Voigt function fitting of (c) and (d). The lines (red and black) are linear fitting to obtain the first-order temperature coefficient.

**S11. Tabulation of the first-order power coefficients, temperature coefficients, and anisotropic in-plane thermal conductivities using mode V for all ReS<sub>2</sub> samples**

ReS <sub>2</sub> samples thickness and their orientation		Power Coefficient (cm <sup>-1</sup> /mW)	Temperature coefficient (cm <sup>-1</sup> /K)	Thermal Conductivity (W/m-K)
2.5 nm (AA)	b-axis	-(10.36 ± 0.36)	-(1.22 ± 0.06) × 10 <sup>-2</sup>	75 ± 6
	Cross b-axis	-(7.17 ± 0.45)	-(0.74 ± 0.05) × 10 <sup>-2</sup>	65 ± 5
3.5 nm (AA)	b-axis	-(10.89 ± 0.22)	-(1.23 ± 0.10) × 10 <sup>-2</sup>	51 ± 5
	Cross b-axis	-(7.99 ± 0.24)	-(0.69 ± 0.02) × 10 <sup>-2</sup>	39 ± 2
3.5 nm (AB)	b-axis	-(12.6 ± 0.40)	-(1.17 ± 0.06) × 10 <sup>-2</sup>	42 ± 3
	Cross b-axis	-(8.45 ± 0.19)	-(0.69 ± 0.03) × 10 <sup>-2</sup>	37 ± 2
5.2 nm (AA)	b-axis	-(8.2 ± 0.26)	-(0.97 ± 0.07) × 10 <sup>-2</sup>	36 ± 3
	Cross b-axis	-(6.59 ± 0.41)	-(0.60 ± 0.06) × 10 <sup>-2</sup>	28 ± 4
8 nm (AB)	b-axis	-(4.61 ± 0.12)	-(1.28 ± 0.03) × 10 <sup>-2</sup>	55 ± 3
	Cross b-axis	-(3.96 ± 0.20)	-(0.95 ± 0.03) × 10 <sup>-2</sup>	48 ± 4

**Table S1.** Using mode V, first-order power coefficients, temperature coefficients, and anisotropic thermal conductivities.

**S12. Tabulation of the first-order power coefficients, temperature coefficients, and anisotropic in-plane thermal conductivities using mode III for all ReS<sub>2</sub> samples**

ReS <sub>2</sub> samples thickness and their orientation		Power Coefficient (cm <sup>-1</sup> /mW)	Temperature coefficient (cm <sup>-1</sup> /K)	Thermal Conductivity (W/m-K)
2.5 nm (AA)	b-axis	$-(6.7 \pm 0.28)$	$-(0.78 \pm 0.05) \times 10^{-2}$	$74 \pm 6$
	Cross b-axis	$-(4.33 \pm 0.12)$	$-(0.46 \pm 0.05) \times 10^{-2}$	$67 \pm 5$
3.5 nm (AA)	b-axis	$-(7.23 \pm 0.19)$	$-(0.76 \pm 0.02) \times 10^{-2}$	$48 \pm 3$
	Cross b-axis	$-(5.87 \pm 0.36)$	$-(0.51 \pm 0.03) \times 10^{-2}$	$39 \pm 5$
3.5 nm (AB)	b-axis	$-(8.67 \pm 0.33)$	$-(0.8 \pm 0.02) \times 10^{-2}$	$42 \pm 3$
	Cross b-axis	$-(5.98 \pm 0.22)$	$-(0.50 \pm 0.01) \times 10^{-2}$	$38 \pm 2$
5.2 nm (AA)	b-axis	$-(5.05 \pm 0.34)$	$-(0.62 \pm 0.04) \times 10^{-2}$	$37 \pm 5$
	Cross b-axis	$-(3.79 \pm 0.12)$	$-(0.39 \pm 0.01) \times 10^{-2}$	$31 \pm 2$
8 nm (AB)	b-axis	$-(3.57 \pm 0.10)$	$-(0.96 \pm 0.02) \times 10^{-2}$	$53 \pm 2$
	Cross b-axis	$-(2.74 \pm 0.09)$	$-(0.63 \pm 0.01) \times 10^{-2}$	$45 \pm 2$

*Table S2. First-order power coefficients, temperature coefficients, and anisotropic thermal conductivities using mode III.*

**References**

- (1) Feng, Y.; Zhou, W.; Wang, Y.; Zhou, J.; Liu, E.; Fu, Y.; Ni, Z.; Wu, X.; Yuan, H.; Miao, F.; Wang, B.; Wan, X.; Xing, D. Raman Vibrational Spectra of Bulk to Monolayer ReS<sub>2</sub> with Lower Symmetry. *Phys. Rev. B* **2015**, *92* (5), 054110. <https://doi.org/10.1103/PhysRevB.92.054110>.
- (2) Zhou, Y.; Maity, N.; Rai, A.; Juneja, R.; Meng, X.; Roy, A.; Zhang, Y.; Xu, X.; Lin, J.-F.; Banerjee, S. K.; Singh, A. K.; Wang, Y. Stacking-Order-Driven Optical Properties and Carrier Dynamics in ReS<sub>2</sub>. *Advanced Materials* **2020**, *32* (22), 1908311. <https://doi.org/10.1002/adma.201908311>.
- (3) Zhou, Y.; Maity, N.; Lin, J.-F.; Singh, A. K.; Wang, Y. Nonlinear Optical Absorption of ReS<sub>2</sub> Driven by Stacking Order. *ACS Photonics* **2021**, *8* (2), 405–411. <https://doi.org/10.1021/acsp Photonics.0c01225>.
- (4) Qiao, X.-F.; Wu, J.-B.; Zhou, L.; Qiao, J.; Shi, W.; Chen, T.; Zhang, X.; Zhang, J.; Ji, W.; Tan, P.-H. Polytypism and Unexpected Strong Interlayer Coupling in Two-Dimensional Layered ReS<sub>2</sub>. *Nanoscale* **2016**, *8* (15), 8324–8332. <https://doi.org/10.1039/C6NR01569G>.
- (5) Sahoo, S.; Gaur, A. P. S.; Ahmadi, M.; Guinel, M. J.-F.; Katiyar, R. S. Temperature-Dependent Raman Studies and Thermal Conductivity of Few-Layer MoS<sub>2</sub>. *J. Phys. Chem. C* **2013**, *117* (17), 9042–9047. <https://doi.org/10.1021/jp402509w>.